Journal of ELECTRONIC MATERIALS, Vol. 49, No. 1, 2020
https://doi.org/10.1007/s11664-019-07456-4

TMS2019 MICROELECTRONIC PACKAGING, INTERCONNECT, AND PB-FREE SOLDER

Time Independent Deformation of a Sn-Ag-Bi Pb-Free Solder: Stress–Strain Deformation and Yield Stress Properties

PAUL T. VIANCO,[1,2] BONNIE B. MCKENZIE,[1] JEROME A. REJENT,[1] J. MARK GRAZIER,[1] CELEDONIO E. JARAMILLO,[1] and ALICE C. KILGO[1]

1.—Sandia National Laboratories, P.O. Box 5800, Albuquerque, NM 87185, USA. 2.—e-mail: ptvianc@sandia.gov

This study examined the yield stress and stress–strain deformation of the 91.84Sn-3.33Ag-4.83Bi (wt.%, abbreviated Sn-Ag-Bi) solder as part of an overall effort to develop a computational model for predicting solder joint reliability. These properties were obtained by compression testing and correlated with the role of Bi in the microstructure by scanning electron microscopy. The strain rates were 4.2×10^{-5} s^{-1} and 8.3×10^{-4} s^{-1}. The test temperatures ranged from − 25°C to 160°C. Samples were tested in the as-fabricated condition or following a 24-h aging treatment at either 125°C or 150°C. The yield stress decreased monotonically with test temperature at both strain rates for Sn-Ag-Bi in the as-fabricated condition. The 125°C, 24 h aging treatment increased the yield stress measured at 25°C, 75°C, and 125°C, but left it unchanged at − 25°C and 160°C. The 150°C aging treatment caused a cross-over effect at approximately 30°C and 70°C for the 4.2×10^{-5} s^{-1} and 8.3×10^{-4} s^{-1} strain rates, respectively. Work softening was observed; its source was a combination of continuous dynamic recrystallization and the Portevin–Le Chatelier effect. The latter phenomenon was solely responsible for fluctuations in the stress–strain curves. Significant variations were observed for the Bi-rich structures as a function of aging treatment as well as following deformation, yet yield stress and plastic deformation performance remained predictable under these very high homologous temperatures.

Key words: Tin-silver-bismuth (Sn-Ag-Bi) solder, yield stress, isothermal aging, constitutive model

INTRODUCTION

Medium and Low Melting Temperature Solders

Medium and low melting temperature, lead (Pb)-free solders are attracting attention in the electronics industry. The lower solidus and liquidus temperatures allow for reduced process temperatures that minimize thermal degradation to printed circuit boards (PCBs) or damage to heat-sensitive components.[1] The medium melting temperature, Pb-free solders include the ternary composition, 91.84Sn-3.33Ag-4.83Bi (wt.%, abbreviated Sn-Ag-Bi).[2] Several solderability and reliability studies have been performed on this composition as well as quaternary modifications by adding copper (Cu), nickel (Ni), etc.[3–11] Recent studies confirmed that Sn-Ag-Bi-based solders have stable mechanical properties under thermal mechanical fatigue (TMF), resulting in an improvement to the long-term reliability of printed wiring assembly (PWA) interconnections.[12–14]

The low melting temperature, Pb-free solders are based on the composition of eutectic 58Bi-42Sn (eutectic temperature, 139°C). This solder was considered for PWAs in several early studies.[5,6,15] The 58Bi-42Sn solder exhibited excellent solderability and PWA-level reliability. However, solid-state

(Received May 10, 2019; accepted July 17, 2019; published online July 29, 2019)

aging tests, which documented intermetallic compound (IMC) layer growth, determined that 58Bi-42Sn/Cu interconnections could fail prematurely by brittle fracture.[16] Ternary modifications, which include silver (Ag), Cu and indium (In) additions, are showing promising results.[17–19]

Computational Modeling Development

Computational models provide an important tool for predicting solder joint reliability under TMF, shock, and vibration conditions. The time-independent (stress–strain) and time-dependent (creep) mechanical properties are used to develop a unified creep-plasticity (UCP) constitutive equation that underlies these models.[20,21] Compression testing has determined the mechanical properties that enabled the development of a UCP equation for several Pb-free solders.[22–25]

The development of a UCP constitutive equation for the Sn-Ag-Bi solder began with documenting its creep properties.[26] The test temperatures were in the range of − 25°C to 160°C. Creep data were obtained from specimens in the as-fabricated (cast) condition as well as following 24-h aging treatments at either 125°C or 150°C. Based upon the "sinh law" analysis methodology, the time exponent (n) and apparent activation energies (ΔH) were:

- As-fabricated: $n = 3.1 \pm 0.4$ and ΔH 66 ± 7 kJ/mol;
- Aged at 125°C (24 h): $n = 2.2 \pm 0.5$ and $\Delta H = 54 \pm 7$ kJ/mol, and
- Aged at 150°C (24 h): $n = 2.2 \pm 0.5$ and ΔH 56 ± 8 kJ/mol.

The aging treatments caused only small decreases in the mean values of n and ΔH that were within experimental error, which indicated a desired stability when the Sn-Ag-Bi is used at a high homologous temperature, T_h, which is equal to the ratio: $T_{environment}/T_{solidus}$, with all values in degrees Kelvin (K).

D. Witkin performed creep tests on the Sn-Ag-Bi alloy over a more limited temperature range of 42–125°C and stresses of 3.5–60 MPa (20–90% of the yield strength).[27] The author used the double-lap shear *solder joint* test specimen. Despite the different test configuration, Witkin obtained very similar sinh law parameters that did not change significantly following the aging treatment of 150°C for 336 h.

The same author preformed stress–strain tests on the Sn-Ag-Bi solder.[28] Tension tests were performed using a cylindrical, dog-bone sample geometry and strain rate of 8.3×10^{-4} s^{-1}. The test temperatures were 25°C, 75°C, and 125°C and sample conditions of as-fabricated or following an aging treatment at 150°C for 336 h. The yield stress values, which represented the as-fabricated condition, were 58.3 MPa (25°C), 46.1 MPa (75°C), and 38.4 MPa (125°C). The values were not changed significantly by the aging treatment. Unfortunately, these data were insufficient to support the development of a UCP equation. The Witkin study also compared the yield strengths between Sn-Ag-Bi and the Sn-3.4Ag-1.0Cu-3.3Bi alloy. The tests results did not indicate a significant difference between them. This finding implies that the UCP equation and associated computational model developed for the Sn-Ag-Bi solder, would provide a suitable approximation of the behavior of the higher-order Sn-Ag-Bi-X compositions.

The objective of the present study was to more completely document the time-independent deformation behavior of the Sn-Ag-Bi alloy. The compression test methodology was used to obtain the yield stress as a function of test temperature, strain rate, and aging condition. The true stress/true strain curves were used to analyze the post-yield point, plastic deformation behavior. The findings will be combined with the creep properties described in reference 26 to complete the UCP equation. Lastly, both yield stress and plastic deformation were correlated to the solder microstructure as documented by the scanning electron microscope (SEM).

EXPERIMENTAL PROCEDURE

Test Samples

The solder alloy had the composition: 91.84Sn-3.33Ag-4.83Bi (wt.%). Compression tests was performed on right cylindrical samples having the nominal dimensions of 10 mm diameter and 19 mm length. These dimensions established a length-to-diameter (L/D) ratio of 2.0, which is considered "short" per the ASTM E9-89A specification.[29] The compression test methodology was selected in order to capture the effects of extended plastic deformation prior to failure. A detailed description is provided in reference 25 of the sample fabrication equipment and procedures. The authors note that, although the precise cooling rate value was not recorded for the casting process, the subsequent quantitative measurements in this study and those prior to it, attested to the *consistency* of the microstructure.

The specimens were tested in the as-cast condition or after aging for 24 h at one of two temperatures: 125°C or 150°C. All aging treatments were performed in air. Duplicate samples were run under each of the aging conditions and test parameters.

Stress–Strain Tests

The stress–strain experiments were performed on a servo-hydraulic test frame. The test temperatures were (± 0.5°C): − 25°C, 25°C, 75°C, 125°C, and 160°C, using one of two strain rates: 4.2×10^{-5} s^{-1} and 8.3×10^{-4} s^{-1}. These strain rates were selected

because they are representative of time independent deformation that contributes to thermal mechanical fatigue (TMF). The load–displacement data were converted to true stress-true strain values. The yield stress was determined by the 0.2% offset criterion.[29]

The static Young's modulus would ordinarily be determined from the linear segment of the stress–strain curve per the ASTM E111-82 specification.[30] However, the right-cylinder geometry causes such measurements to be very sensitive to specimen alignment within the load train of the test frame.[31] The ASTM E9-89A standard recommends an L/D of no less than eight (8) for this measurement. Unfortunately, that high ratio causes the test specimen to be susceptible to buckling during post-yield point deformation. Therefore, the Sn-Ag-Bi elastic modulus was measured dynamically, using sound waves per the ASTM-E1876 standard.[32] Those data, together with the measurements of the coefficient of thermal expansion (CTE) will be presented in a follow-up report along with the UCP constitutive model.

Microstructure Analysis

The microstructures were documented using the scanning electron microscope (SEM). The secondary electron (SE) image mode showed the distribution of Ag_3Sn particles while the back-scattered electron (BSE) image mode optimized the identification of Bi particles. The transmission electron microscopy (TEM) would be required to study the Bi atoms in solid-solution; however, this level of analysis was beyond the scope of this work as was also a rigorous, quantitative analysis of phase particle size distributions.

RESULTS

Solder Microstructures: As-Fabricated and Post-aged Conditions

The microstructural analysis began with the as-fabricated condition. The Ag_3Sn phase particles are highlighted in Fig. 1a. Their distribution was similar to that of other high-Ag, Sn-Ag-based alloys.[22] Larger Bi particles are shown in Fig. 1b, using the SEM/BSE image mode of the same area as in Fig. 1a. The Sn-rich matrix, which had Bi in solid-solution and is designated as Sn(Bi) is shown by the high-magnification, SEM/BSE image in Fig. 1c; the area is designated by the white box of Fig. 1b. Several Bi precipitate particles are noted in the photograph (white arrow). Electron probe microanalysis (EPMA) determined that the solid-solution composition contained 3.7 ± 0.2 wt.% Bi.

The Sn-Ag-Bi microstructure is shown in Fig. 2 following the aging treatment at 125°C for 24 h. Figure 2a highlights the Ag_3Sn particles; their size and distribution were not significantly different from the as-fabricated condition. Figure 2b

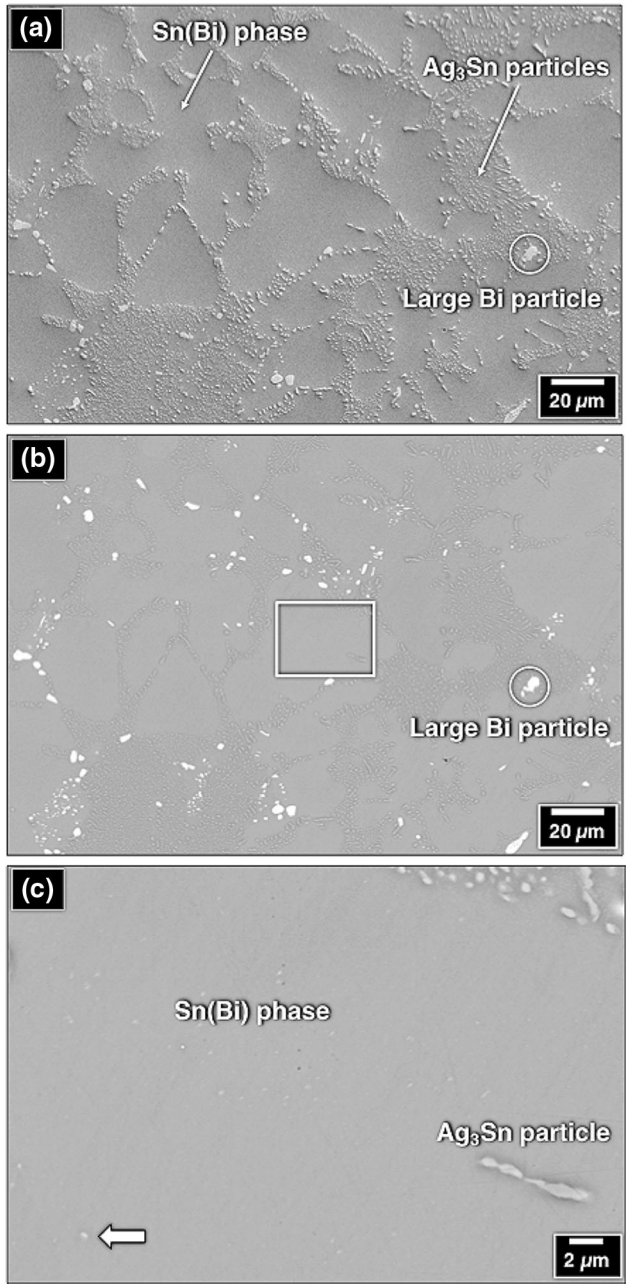

Fig. 1. SEM photographs show the microstructure of the Sn-Ag-Bi solder in the as-fabricated condition: (a, b) low magnification, SEM/SE and SEM/BSE images, respectively, of the same area. The three primary phases are identified in (a). (c) High magnification BSE image shows the area outlined by the white box in (b). The white arrow identifies a Bi particle, many of which were scattered in the Sn(Bi) phase.

accentuates the larger Bi precipitates, which had a slightly reduced presence versus the as-fabricated condition. This trend implied that the aging treatment caused a small degree of *resolutionizing* of Bi back into the Sn(Bi) phase. This hypothesis was confirmed when an EPMA measured a higher Bi concentration of 4.6 ± 0.7 wt.%. In addition, several Sn(Bi) regions showed a higher concentration of Bi precipitates (black arrows). Figure 2c provides a

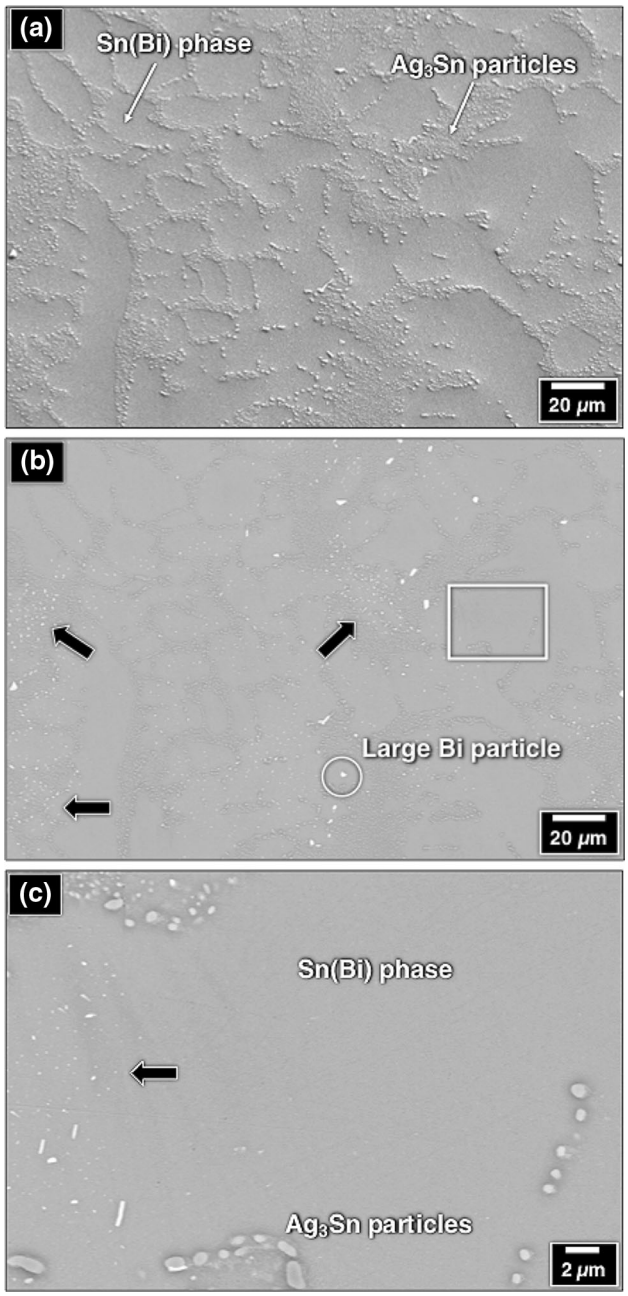

Fig. 2. SEM photographs show the microstructure of the Sn-Ag-Bi solder after aging at 125°C for 24 h: (a, b) low magnification, SEM/SE and SEM/BSE images, respectively, of the same area. The black arrows indicate the few Sn(Bi) regions in which Bi precipitates form. (c) High magnification BSE image shows the area outlined by the white box in (b). The black arrow points to an area of Bi precipitate particles scattered in the Sn(Bi) phase.

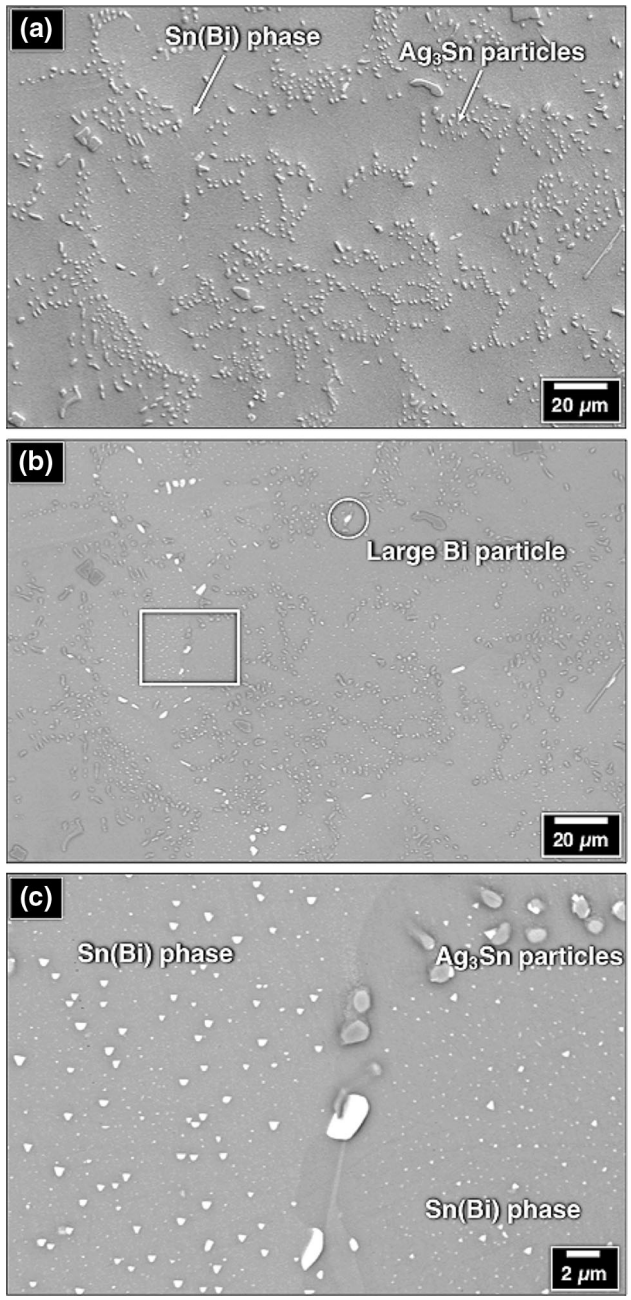

Fig. 3. SEM photographs show the microstructure of the Sn-Ag-Bi solder after aging at 150°C for 24 h: (a, b) low magnification, SEM/SE and SEM/BSE images, respectively, of the same area. (c) High magnification BSE image shows the area outlined by the white box in (b).

high magnification image of the Sn(Bi) matrix identified by the white rectangle in Fig. 2b. The region on the left-hand side exhibits small Bi precipitates (black arrow) while the area on the right-hand side is free of them.

The Sn-Ag-Bi microstructure is shown in Fig. 3 that resulted from the 150°C (24 h) aging treatment. The Ag_3Sn particles coarsened as shown in Fig. 3a. Referring to Fig. 3b, larger Bi particles precipitated around the borders of the Sn(Bi) regions. The area, which is highlighted in the white box, is shown at higher magnification in Fig. 3c. An extensive concentration of Bi precipitates formed in the Sn(Bi) matrix. Nevertheless, the Bi concentration was 4.8 ± 0.6 wt.% in the Sn(Bi) phase, which was not statistically different from that measured after 125°C aging treatment, and implies a retention of resolutionized Bi.

In summary, the Sn-Ag-Bi solder microstructure exhibited Ag_3Sn particles, larger Bi particles, and a

Sn(Bi) solid-solution phase. The 125°C (24 h) aging treatment did not significantly alter the Ag_3Sn particle network. The large Bi particles exhibited a degree of resolutionizing. A few Bi precipitate particles formed in isolated Sn(Bi) solid-solution regions. Aging at 150°C (24 h) caused significant coarsening of the Ag_3Sn and large Bi particles as well as significant Bi precipitation in the Sn(Bi) solid-solution phase.

Lastly, the SEM imaging techniques did not reveal microstructural features that were expressly indicative of recovery processes. Also, the SEM images did not show channeling artifacts that would indicate recrystallization activities after either aging treatment.

Yield Stress Analysis

The yield stress is displayed in Fig. 4 as a function of test temperature for Sn-Ag-Bi solder in the as-fabricated condition. Circles identify data obtained at 4.2×10^{-5} s^{-1}. The open circles are the mean values while the closed circles show the duplicate tests. Squares identify data obtained at 8.3×10^{-4} s^{-1}. The open squares are the mean values of the duplicate tests are indicated by the closed squares. The duplicate values were statistically the same at all conditions with one exception: 125°C test temperature and 8.3×10^{-4} s^{-1} strain rate. The two values were only slightly different, statistically. The corresponding stress–strain curves did not indicate an obvious source for the variability.

The yield stresses decreased with increasing temperature at both strain rates. The trend occurred *monotonically,* which implies an absence of any unanticipated microstructural changes across the test temperatures. The yield stress values were nearly identical at − 25°C between the two strain rates. Strain rate sensitivity became more significant with increasing test temperature because of a faster drop to the yield stress at the slower strain rate.

A comparison was made between the Sn-Ag-Bi solder yield stress values and those measured for the 95.5Sn-3.9Ag-0.6Cu (wt.%, Sn-Ag-Cu) solder.[22] Both samples were in the as-fabricated condition. The two data sets are plotted together in Fig. 5. The Sn-Ag-Bi solder demonstrated significantly higher yield stresses at all temperatures and both strain rates with the exception of tests performed at 160°C and 4.2×10^{-5} s^{-1} where the yield stresses were equivalent to those of the Sn-Ag-Cu solder.

The yield stress data in Fig. 5 shows that the two alloys had different temperature sensitivities. The Sn-Ag-Bi alloy exhibited a difference of yield stress between the two strain rates that increased monotonically with increasing test temperature. On the other hand, the Sn-Ag-Cu solder showed nearly identical yield stresses at 25°C and 75°C for the two strain rates. The yield stresses diverged between

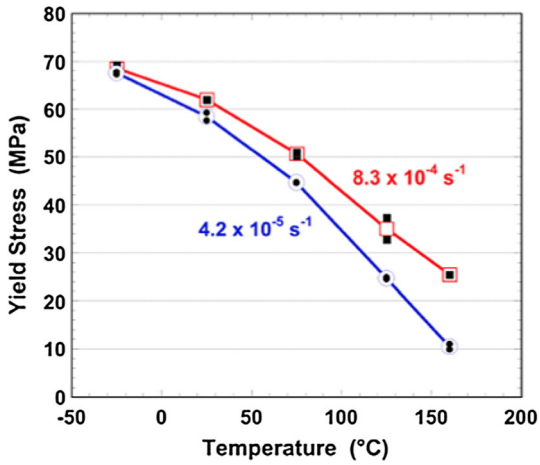

Fig. 4. Yield stress is plotted as a function of temperature for the Sn-Ag-Bi solder in the as-fabricated condition. Circles identify data obtained at 4.2×10^{-5} s^{-1}. The open circles are the mean values of the duplicate tests indicated by the closed circles. Squares identify data obtained at 8.3×10^{-4} s^{-1}. The open squares are the mean values of the duplicate tests indicated by the closed squares.

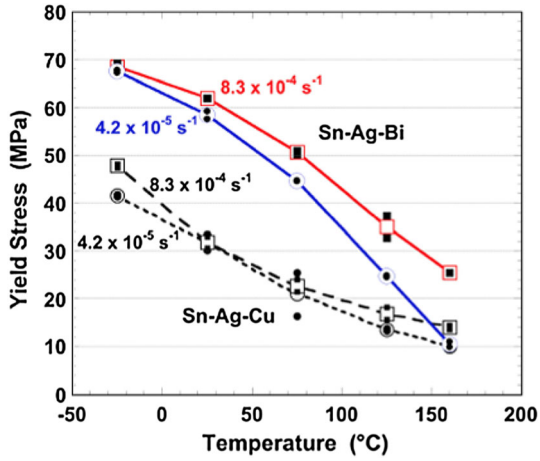

Fig. 5. Yield stress is plotted as a function of test temperature for Sn-Ag-Bi (solid lines) and Sn-Ag-Cu (dashed lines). Both materials were in the as-fabricated condition. Circles identify data obtained at 4.2×10^{-5} s^{-1}. The open circles are the mean values of the duplicate tests, which are indicated by the closed circles. Squares identify data obtained at 8.3×10^{-4} s^{-1}. The open squares are the mean values of the duplicate tests that are indicated by the closed squares.

strain rates towards both lower and higher test temperatures.

The Sn-Ag-Bi yield stresses were compared to tensile test values obtained by Witkin.[28] See Table - I. Both data sets were obtained under similar test parameters: as-fabricated sample condition; 8.3×10^{-4} s^{-1} strain rate; as well as 25°C, 75°C, and 125°C temperatures. The Witkin study showed slightly lower yield stresses at 25°C and 75°C, but a comparable value at 125°C. Error bars were not included in the reference 28 data.

Table I. Yield strength comparison between present study and Witkin. Data was obtained from Ref. [28]

	Yield strength (MPa) ($d\varepsilon/dt = 8.4 \times 10^{-4}$ s^{-1})			
	Present study		Witkin study (2013)[a]	
Test temperature (°C)	Aged: As-fabricated 150°C, 24 h		Aged: As-fabricated 150°C, 336 h	
25	62.0, 62.1	56.2, 56.4	58.3	55.4
75	50.3, 51.1	51.7, 52.3	46.1	46.3
125	32.8, 38.6	41.4, 42.7	38.4	38.2

[a]Values are the average of three or four tests.

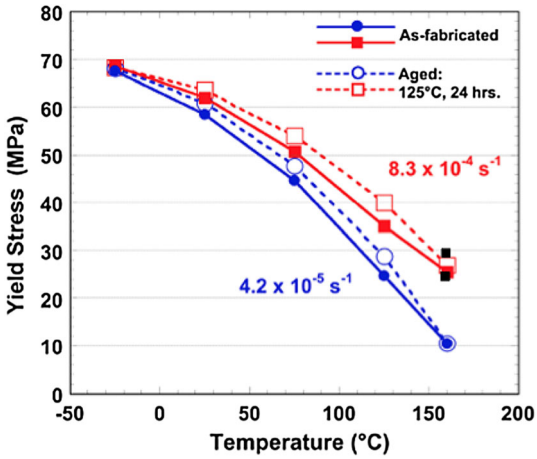

Fig. 6. Yield stress is shown as a function of test temperature, strain rate, and the as-fabricated versus 125°C, 24 h aging sample conditions. Individual test points fell within the symbol size (mean value) except for the post-aged sample, which was tested at 160°C and 8.3 × 10^{-4} s^{-1}. The duplicate test data are shown by the closed squares for the latter case.

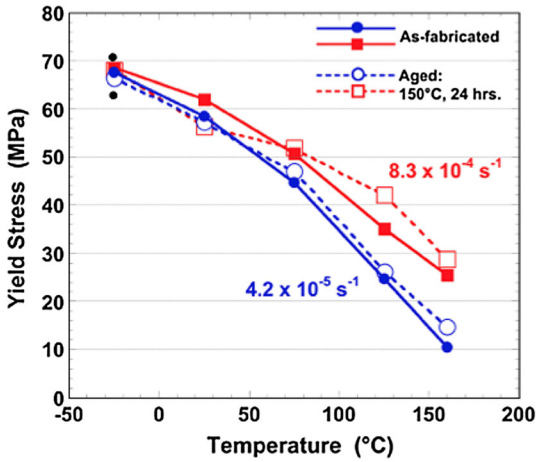

Fig. 7. Yield stress is shown as a function of test temperature, strain rate, and the as-fabricated versus 150°C, 24 h aging sample conditions. Individual test points fell within the symbol size (mean value) except for the post-aged sample, which was tested at − 25°C and 4.2 × 10^{-5} s^{-1}. The duplicate test data are shown by the closed circles for the latter case.

The yield stress data were examined as a function of temperature and strain rate for Sn-Ag-Bi samples aged at 125°C (24 h) prior to compression testing. The mean values are plotted in Fig. 6. The closed symbols represent the as-fabricated condition and the open symbols refer to the aged samples. The individual test measurements fell within the mean symbol size with one exception, the aged sample tested at 160°C and 8.3 × 10^{-4} s^{-1}. In the latter case, the individual test values are shown by the closed squares. Identical trends prevailed between the two sample conditions. The yield stresses were "anchored" at − 25°C where *all* values were identical. The yield stresses diverged between strain rates with increasing test temperature for both sample conditions. The aging treatment delivered higher yield stresses at 25°C, 75°C and 125°C for both strain rates. The yield stress enhancement provided by the aging treatment was subsequently lost at 160°C for both strain rates.

Figure 7 compares yield stresses between samples in the as-fabricated condition versus those that were aged at 150°C for 24 h. The format is the same as that used in Fig. 6. The duplicate test values were within each symbol size (mean value) with the exception of the test point: − 25°C, post-aged condition, and 4.2 × 10^{-5} s^{-1} strain rate; those individual tests are represented by closed circles. As observed in Fig. 6, the yield stress values were the same at − 25°C, regardless of aging condition or strain rate. The aged samples had their yield stress decrease with increasing test temperature at both strain rates. Superimposed on that trend was a second phenomenon that was observed at both strain rates, but was statistically significant only at the faster strain rate. At the test temperature of 25°C, the mean yield stress was less for the aged samples. Then, the yield stress of the aged samples crossed over at approximately 30°C and 75°C for the 4.2 × 10^{-5} s^{-1} and 8.3 × 10^{-4} s^{-1} strain rates,

respectively, to become greater than that of the as-fabricated specimens at the higher test temperatures.

The yield strength data were compared to the post-aged results reported by Witkin.[28] Again, the reader is referred to Table I. The aging temperature used by Witkin was also 150°C; however, the aging duration was considerably longer at 336 h. The strain rate was 8.3×10^{-4} s^{-1}. Beginning with the 25°C test temperature, Witkin's data showed a smaller decrease of yield stress (– 5%) between the as-fabricated and aged conditions versus the over 9% loss observed in the present study. Since both studies showed similar yield stresses after aging, it is possible that the Witkin samples had been "partially aged" during fabrication, resulting in a reduced, as-fabricated yield stress.

At 75°C (Table I), the present study showed higher yield strengths when the latter were compared to the Witkin data. However, in both studies, the yield stress changed very little between the respective as-fabricated and aged conditions, despite the different aging times. In the present study, the similar yield stresses were attributed to the "crossover" effect noted above. A similar behavior appears to have taken place between the 25°C and 75°C data of the Witkin study. However, the Witkin results show nearly identical yield stresses at 125°C, which does not support a "cross-over" effect in those tests. This observation suggests that the longer time duration of 336 h (150°C) caused an "overaging" effect that mitigated the yield stress improvement observed after 24 h aging duration of the current study.

A comparison was made between the yield stresses of the Sn-Ag-Bi and Sn-Ag-Cu solders that included all three aging conditions. Figure 8 combines the data from both alloys for the strain rate of 4.2×10^{-5} s^{-1}. Trend lines, which show the mean values, simplify the visualization. The error bar represents the scatter observed in these data. Generally, the aging treatments increased the yield stress of the Sn-Ag-Bi solder with the exception of test temperatures less than the crossover point (30°C). The Sn-Ag-Cu alloy experienced a yield stress decrease due to the aging treatments. A similar comparison was made between the two solders, but addressing the faster strain rate of 8.3×10^{-4} s^{-1}. The combined data are presented in Fig. 9. The same general trends were observed here as were recorded at the slow strain rate. The crossover effect is observed for the Sn-Ag-Bi alloy (≈ 70°C). Although the post-aging yield stresses of the Sn-Ag-Cu solder remained less than those of the as-fabricated condition, the two trend lines were closer together under the faster strain rate. Since both solder compositions incorporate similar Ag_3Sn particle concentrations and morphologies, the different trends observed in Figs. 8 and 9 are attributed to the Bi content of the Sn-Ag-Bi solder.

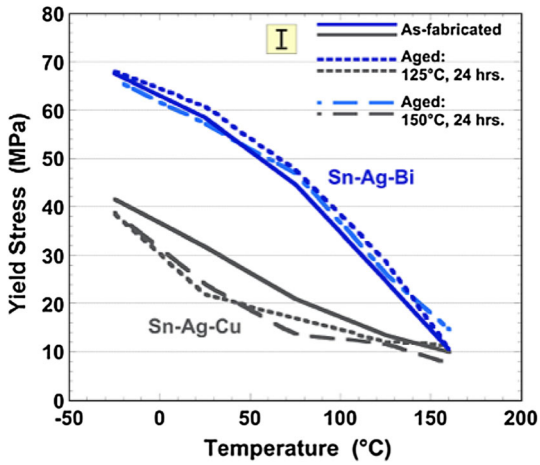

Fig. 8. Mean yield stress is shown as a function of test temperature and aging condition for the Sn-Ag-Bi and Sn-Ag-Cu solders. The strain rate is 4.2×10^{-5} s^{-1}. The sample conditions are designated as follows: as-fabricated, solid lines; aged at 125°C (24 h), short dashed lines; and aged at 150°C (24 h), long dashed lines. The error bar is representative of the scatter between duplicate tests.

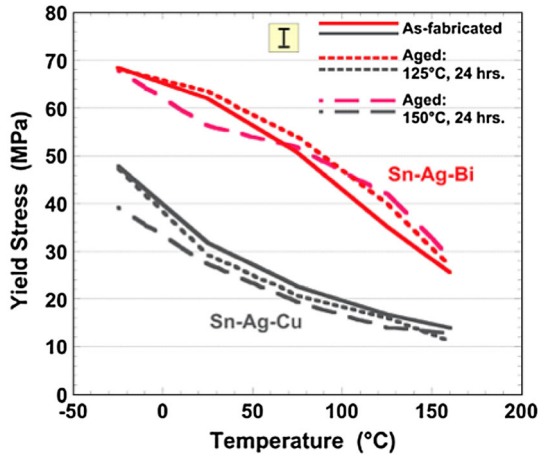

Fig. 9. Mean yield stress is shown as a function of test temperature and aging condition for the Sn-Ag-Bi and Sn-Ag-Cu solders. The strain rate is 8.3×10^{-4} s^{-1}. The sample conditions are designated as follows: as-fabricated, solid lines; aged at 125°C (24 h), short dashed lines; and aged at 150°C (24 h), long dashed lines. The error bar is representative of the scatter between duplicate tests.

Stress–Strain Curves

Shown in Fig. 10a are one of the duplicate true stress-true strain curves that were obtained from each test temperature. The duplicate curves were identical to one-another to within the experimental error. The samples were in the as-fabricated condition and the strain rate was 4.2×10^{-5} s^{-1}. Work hardening was observed throughout the post-yield point, plastic deformation at – 25°C, 25°C, and 75°C. The work hardening rate decreased with increasing temperature. The plastic deformation, which occurred at 125°C and 160°C, is shown Fig. 10b using an expanded *y*-axis scale. A small

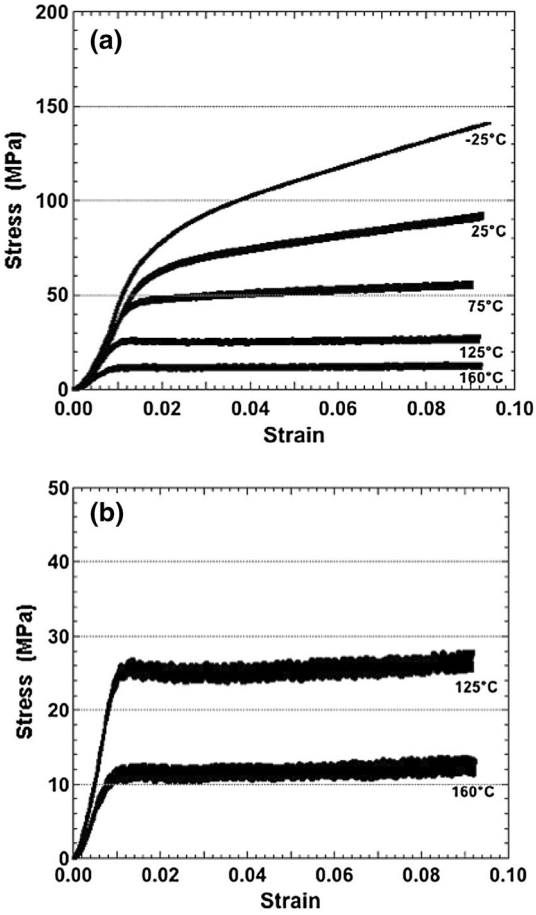

Fig. 10. (a) Representative stress–strain curves are shown as a function of test temperature for samples in the as-fabricated condition. The strain rate was 4.2×10^{-5} s^{-1}. (b) Stress–strain curves are shown for samples tested at 125°C and 160°C using an expanded *y*-axis scale.

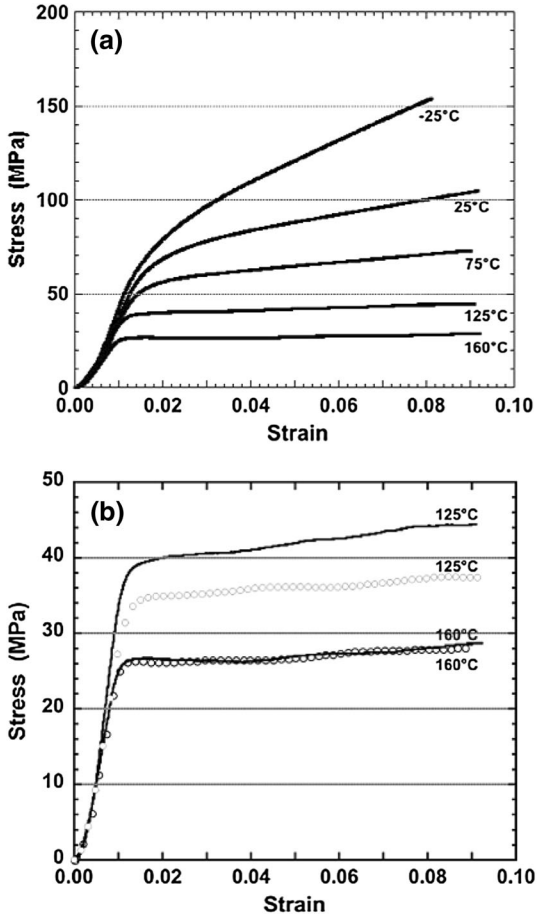

Fig. 11. (a) Representative stress–strain curves are shown as a function of test temperature for samples in the as-fabricated condition. The strain rate was 8.3×10^{-4} s^{-1}. (b) The duplicate stress–strain curves are provided for samples tested at 125°C and 160°C using an expanded *y*-axis scale; they are represented by the solid line and open circles.

degree of work softening immediately followed the yield point. In both cases, the work softening gave way to work hardening when the strains exceeded 0.03. Both the work softening and hardening were more prominent at 125°C.

Representative stress–strain curves are shown in Fig. 11a that were generated at the faster strain rate of 8.3×10^{-4} s^{-1} and all test temperatures. The test specimens were in the as-fabricated condition. The samples tested at − 25°C, 25°C and 75°C clearly exhibited only work hardening. The duplicate stress–strain curves are shown in Fig. 11b representing the 125°C and 160°C test temperatures using an expanded *y*-axis scale. The duplicate plots were shown because they differed significantly at 125°C; the two curves were nearly identical at 160°C. A slight degree of work soften was observed only at 160°C. Otherwise, the tests at both temperatures resulted in fluctuations superimposed on a general trend of work hardening.

The stress–strain curves are shown in Fig. 12 for Sn-Ag-Bi as a function of aging treatment and test temperature. The strain rate was 4.2×10^{-5} s^{-1}. Both aging treatments increased the work hardening rate to an identical degree at − 25°C versus the as-fabricated condition. At 25°C, the two aging treatments produced only slightly faster work hardening rates when compared the as-fabricated condition. The same trend was also observed at 75°C, albeit with a reduced difference of work hardening rate between the three conditions. At 125°C and 160°C, the post-yield point, plastic deformation behaviors were essentially unchanged between all sample conditions.

The stress–strain curves are documented in Fig. 13 that were obtained at the faster strain rate of 8.3×10^{-4} s^{-1}. As observed in Fig. 12, when stress–strain tests were performed at − 25°C, 25°C, and 75°C, the specimens exhibited slightly greater work hardening after the aging treatments versus the as-fabricated condition. The difference was less dramatic at − 25°C than was observed at the slow strain rate. The effect of the aging treatments on the work hardening rate diminished with increasing test temperature as similarly observed at the slower strain rate.

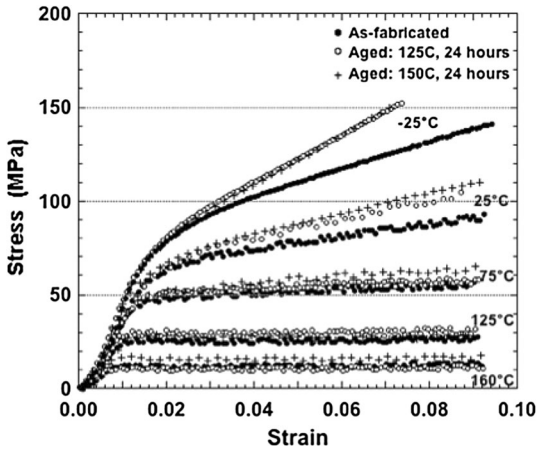

Fig. 12. Stress-strain curves are shown as a function of test temperature that represent all three aging conditions and were tested at 4.2×10^{-5} s^{-1}. The data symbols are as follows: as-fabricated, closed circles; aged at 125°C (24 h), open circles; and aged at 150°C (24 h), crosses.

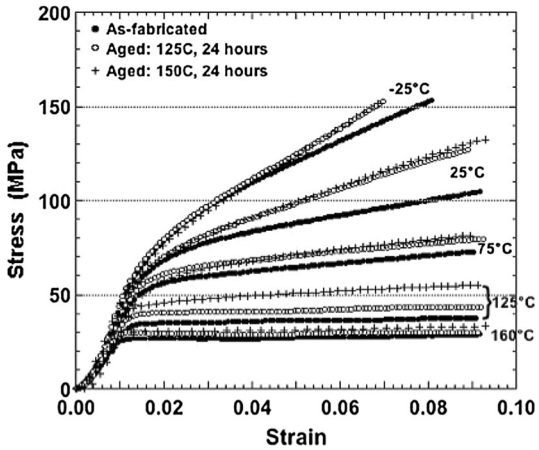

Fig. 13. Stress-strain curves are shown as a function of test temperature that represent all three aging conditions and were tested at 8.3×10^{-4} s^{-1}. The data symbols are as follows: as-fabricated, closed circles; aged at 125°C (24 h), open circles; and aged at 150°C (24 h), crosses.

Greater scrutiny was given to the curves obtained at 125°C because the three plots diverged from one-another in Fig. 13. These data, together with the curves obtained at 160°C, are shown in Fig. 14 using an expanded *y*-axis. An increase of yield stress with aging temperature (Fig. 6) was largely responsible for the difference between the as-fabricated and 125°C, 24 h aged samples; the general work hardening behaviors were similar. However, the 150°C aging temperature caused both an increase of yield stress ("crossover" effect in Fig. 7) as well as an increase of work hardening rate. Fluctuations were superimposed on the work hardening trends of the curves generated by the as-fabricated and post-125°C (24 h) aged samples. The work softening as well as fluctuations were lost when the samples was aged at 150°C, having been replaced with only the work hardening trend. Similar trends were

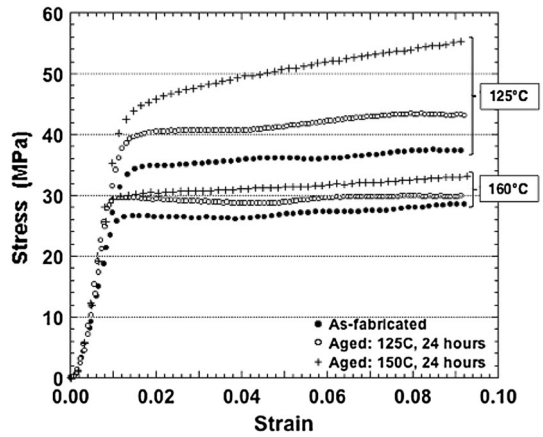

Fig. 14. Representative stress–strain curves show the effect of aging treatments when tests were performed at 125°C and 160°C. The strain rate was 8.3×10^{-4} s^{-1}. The data symbols are as follows: as-fabricated, closed circles; aged at 125°C (24 h), open circles; and aged at 160°C (24 h), crosses.

observed for samples tested at 160°C, but with reduced magnitudes. The closer proximity of the curves to one another is due in part to similar yield stresses (Fig. 9).

Solder Microstructures: Post-deformation

The Sn-Ag-Bi microstructures were documented at the completion of the stress–strain tests to determine the effect(s) of deformation. The visualization was provided by means of a two-by-two matrix of SEM images that represented the two strain rates and two test temperature extremes, – 25°C and 160°C. The images were selected to represent general microstructural trends.

Figure 15 shows low-magnification, SEM/SE images of the post-deformation microstructure belonging to samples that were tested in the as-fabricated condition. Large-scale deformation features such as shear bands, voids, or cracks were not observed in the solder. *The latter observation applied to all of the test samples.* The Ag_3Sn particles did not undergo further coarsening across all four test conditions when a comparison was made to Fig. 1a. This trend also prevailed in samples that were tested after one of the two aging treatments. Therefore, further observations focused on changes to the large Bi particles and the Sn(Bi) phase microstructure.

The SEM/BSE images in Fig. 16 highlight the larger Bi particles. Similar sizes and concentrations were observed in three of the four cases. Those three cases mirrored the untested microstructure in Fig. 1b. The exception was the specimen tested at 4.2×10^{-5} s^{-1} strain rate and 160°C in which coarsening was observed by the large Bi particles.

Changes to the solid-solution Sn(Bi) matrix were documented by the high magnification, SEM/BSE images in Fig. 17. The comparable image of the

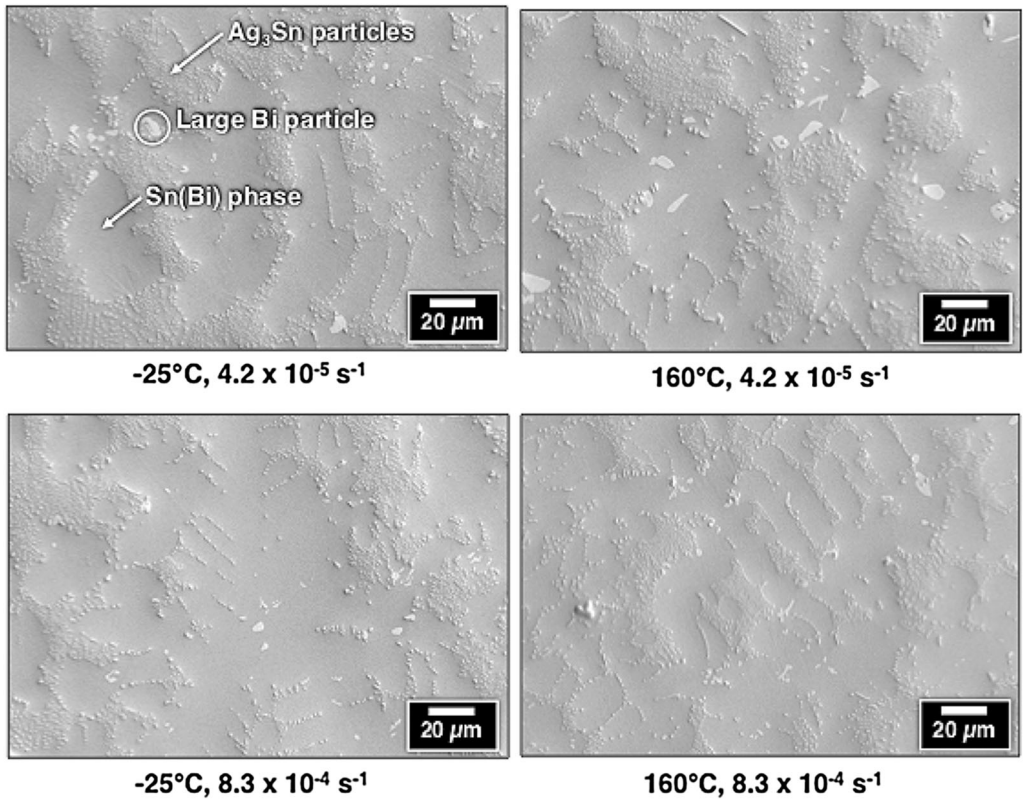

Fig. 15. SEM images show the post-test microstructure of the as-fabricated Sn-Ag-Bi solder obtained at the test temperatures of − 25°C and 160°C and both strain rates. The low magnification, SE mode accentuated the Ag_3Sn particles.

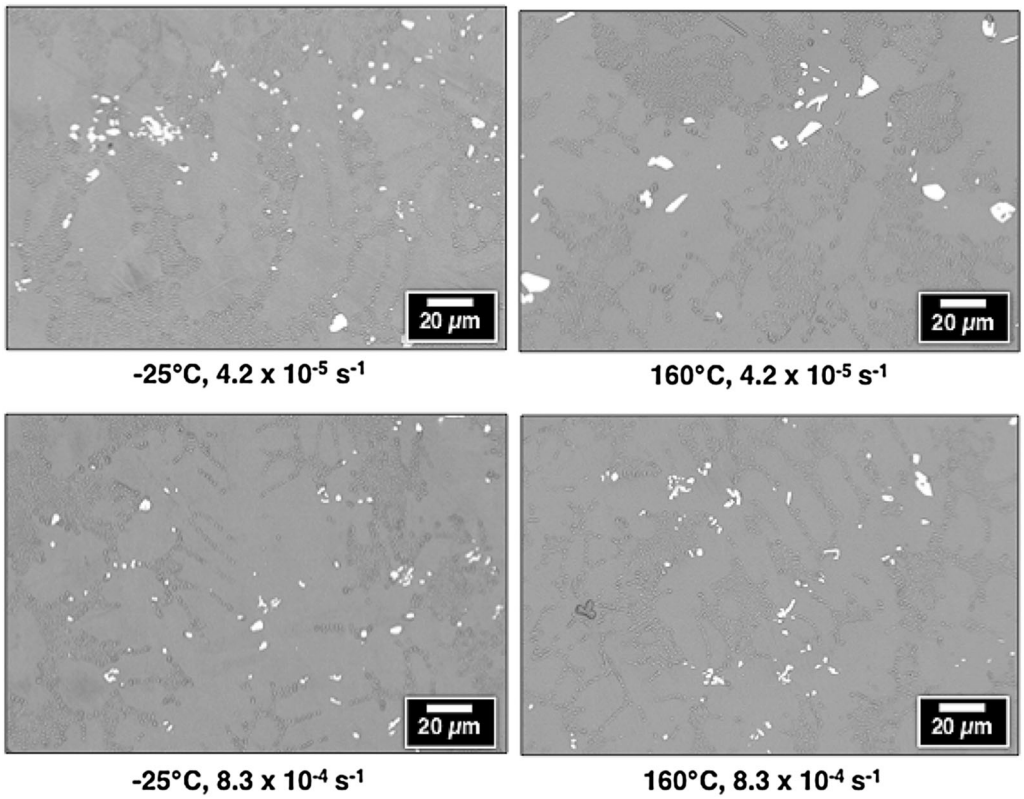

Fig. 16. SEM images show the post-test microstructure of the as-fabricated Sn-Ag-Bi solder obtained at the test temperatures of − 25°C and 160°C and both strain rate. The low magnification, BSE images accentuated the distribution of larger Bi precipitates.

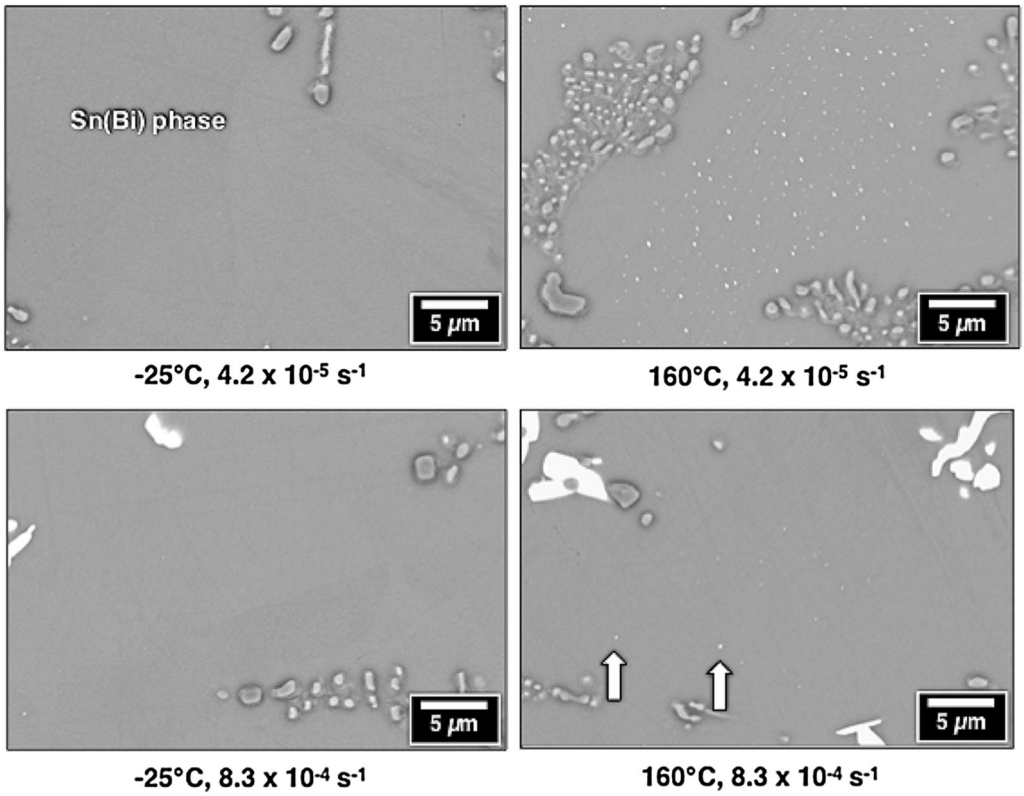

Fig. 17. SEM images show the post-test microstructure of the as-fabricated Sn-Ag-Bi solder obtained at the test temperatures of − 25°C and 160°C and both strain rates. The high magnification BSE images show the Sn(Bi) solid-solution phase. The white arrows indicate the appearance of Bi particles.

untested microstructure appeared in Fig. 1c. The precipitation of Bi particles was negligible after the two tests performed at − 25°C. However, numerous Bi particles was observed following the test performed at 160°C and 4.2×10^{-5} s^{-1} strain rate that were not observed in Fig. 1c. A similar behavior occurred after testing at 8.3×10^{-4} s^{-1} and 160°C (white arrows), but to a considerably lesser magnitude.

The post-yield deformation microstructures were also examined for those test specimens that were aged prior to the stress–strain test. The expressed objective was to determine whether the aging treatments caused the Sn-Ag-Bi microstructure to respond differently to the deformation. Aside from coarsening after aging at 150°C for 24 h, the Ag_3Sn particles were not changed significantly by the deformation under any of the test conditions. Therefore, the discussion focused, again, on changes to the large Bi particles and the Sn(Bi) solid-solution phase.

An analysis began by examining the effects of the 125°C, 24 h aging treatment. Large Bi particles developed from what was initially, the slightly resolutionized microstructure shown in Fig. 2b. This observation is illustrated in Fig. 18a, using the case of a − 25°C test temperature and 4.2×10^{-5} s^{-1} strain rate, which was representative of the next three test temperatures. These results imply that the resolutionizing effect of the aging treatment was reversed by the deformation. When the test temperature was increased to 160°C, Bi precipitates were observed in the Sn(Bi) regions following the slow strain rate deformation. See Fig. 18b. However, only a few Bi particles were identified in the Sn(Bi) phase after deformation at the fast strain rate, which suggests that in situ aging was a likely cause for the Bi precipitates in Fig. 18b.

The aging treatment of 150°C (24 h) caused a more significant response by the large Bi particles to plastic deformation. Therefore, all four matrix images were included in Fig. 19. The samples, which were tested at − 25°C and either strain rate, showed a marked increase in the presence of large Bi particles versus the untested condition (Fig. 3b). When the test temperature was raised to 160°C, the Bi particles coarsened and became fewer in number. In situ aging could have supported this trend at the slower strain rate. However, because a similar magnitude of Bi particle coarsening also took place at the faster strain rate, deformation was a contributing factor to the coarsening behavior.

Significant changes were observed for the Sn(Bi) phase when the Sn-Ag-Bi alloy was aged at 150°C (24 h) prior to the stress–strain test. The corresponding matrix of SEM/BSE images is shown in Fig. 20. The starting microstructure appeared in

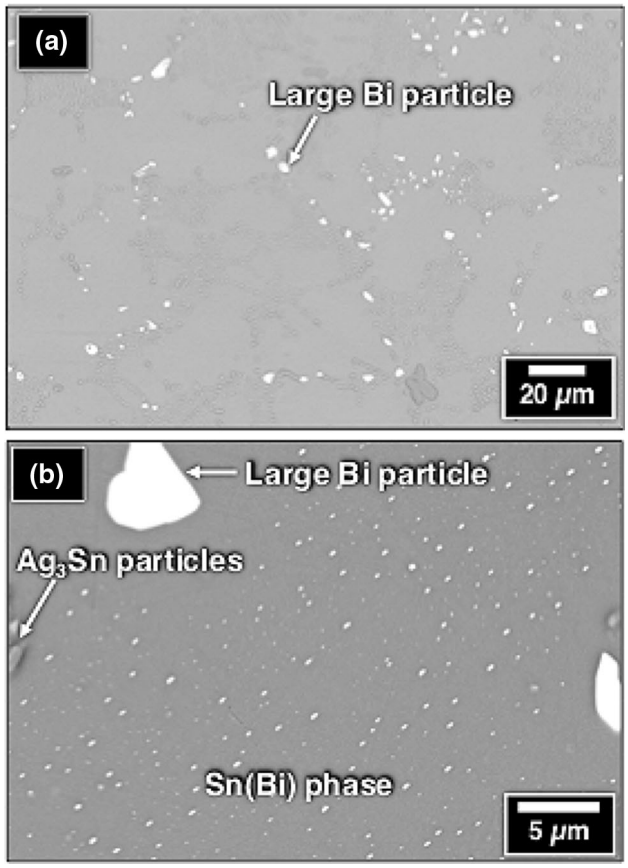

Fig. 18. SEM/BSE image shows the Sn-Ag-Bi microstructure after the stress–strain test was performed at the 4×10^{-5} s^{-1} strain rate. The samples were aged at 125°C for 24 h prior to the test. The (a) image shows the large Bi particles in the sample that completed testing at − 25°C. The (b) image highlights the Sn(Bi) solid-solution phase of the sample following testing at 160°C.

Fig. 3c. The clear difference between Figs. 3c and 20 is the absence of Bi particles from Sn(Bi) phase after the stress–strain tests were performed at − 25°C and either strain rate. When the test temperature was raised to 160°C, a few Bi particles appeared in the Sn(Bi) phase, but far fewer than were observed prior to deformation (Fig. 3c). This trend implies that deformation actually eliminated the Bi precipitates in this instance. Since more particles were present after the slow strain rate than following the fast strain rate, in situ aging cannot be entirely ruled out—however, it was a second-order effect.

DISCUSSION

The discussion is separated into two sections. The first section considers the yield stress data. That analysis includes the microstructures representing the (untested) as-fabricated and post-aged conditions because they would directly impact the yield stress trends. The second section examines the stress–strain curves and their correlation to the post-deformation microstructures. The two sections begin with an analysis of the as-fabricated condition, which is then followed by addressing the aged samples.

Yield Stress

As-Fabricated Condition

The yield stress data were presented in Fig. 4 for Sn-Ag-Bi. The yield stress was identical at − 25°C between the two strain rates. The yield stress reflects the mobility of existing dislocations as well as the creation of additional mobile dislocations, in response to the stress. Since − 25°C still represents a relatively high T_h of 0.51, some degree of thermal activation would assist dislocation mobility. This behavior suggests that few mobile dislocations existed, and/or few mobile dislocations were created, from the starting microstructure (Fig. 1) at the two strain rates. The insensitivity to strain rate diminished with increased test temperature, which implies that thermal activation improved the mobility of existing dislocation, or the creation of additional mobile dislocations.

The yield stress decreased monotonically with increasing temperature. The loss was faster at the slower strain rate because thermal activation becomes more effective under the slower dislocation movement. The magnitude of the yield stress loss was relatively high in Fig. 4 when compared to other common metals and alloys under comparable homologous temperatures. In situ aging at the early stages of the tests was unlikely because sample heat-up was very rapid. Therefore, it was concluded that thermal activation quickly became more effective towards supporting diffusion-assisted mechanisms—broadening of dislocation bows between particles or dislocation climb—at these high homologous temperatures. Also, the data in Fig. 4 confirmed the absence of anomalous phenomena in the microstructures, such as phase changes, short-range ordering, etc. during deformation.

The Sn-Ag-Bi yield stress data were compared to results obtained from the Sn-Ag-Cu alloy in Fig. 5. The two alloys have similar precipitation hardening mechanisms generated by the corresponding Ag_3Sn particles (Fig. 1a). An additional precipitation hardening component is present in the Sn-Ag-Bi alloy due to the large Bi particles (Fig. 1b). But, the latter Bi particles were expected to have a lesser effect because of their reduced number in the microstructure. Therefore, the higher yield stress of the Sn-Ag-Bi solder was attributed primarily to solid-solution strengthening by Bi in the Sn(Bi) phase (Fig. 1c).

Solid-solution strengthening by the Bi atoms was gradually lost with increasing temperature. At the 160°C, the yield stress of the Sn-Ag-Bi solder became equivalent to that of the largely precipitation-strengthened, Sn-Ag-Cu alloy at the slower strain rate. This comparison established the upper temperature limit to the efficacy of the Bi solid-solution strengthening mechanism. The Sn-Ag-Bi

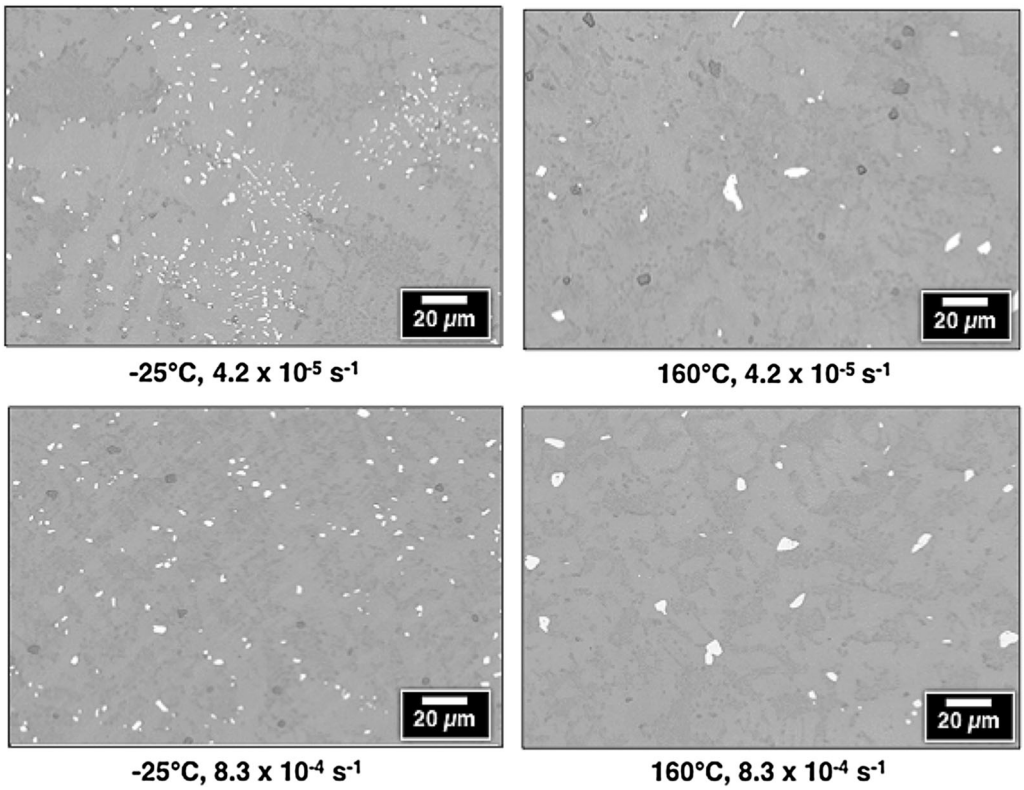

Fig. 19. SEM images show the microstructure of the Sn-Ag-Bi solder obtained at the test temperature extremes of − 25°C and 160°C and both strain rates. The BSE image mode and low magnification accentuated the distribution of larger Bi precipitates. The samples were aged at 150°C for 24 h prior to testing.

solder still retained its yield stress advantage derived from the solid-solution mechanism at the faster strain rate. In summary, the Sn-Ag-Bi solder maintained a significant yield stress advantage versus the Sn-Ag-Cu alloy over the temperature range of − 25°C to 125°C. At the 160°C temperature, the Sn-Ag-Bi solder performed comparably to the Sn-Ag-Cu solder, implying that the Ag_3Sn precipitation hardening mechanism largely controlled the Sn-Ag-Bi yield stress.

A review was made of yield stress data from conventional solid-solution alloys. The Sn-Ag-Bi test (and use) temperatures of − 25°C to 160°C correspond to homologous temperatures in the range of 0.51–0.89. There are few metals and alloys that are tested, let-alone used, at such high homologous temperatures. Traditional solid-solution strengthened materials include the so-called "light alloys," which are based upon Al, Mg, and Mg–Al compositions, as well as numerous high-temperature, Fe- and Ni-based alloys.[32–38] These studies can provide some background information on the effects of aging and solid solution strengthening. However, these materials are typically tested and used at lower homologous temperatures that are in the range of 0.32–0.67. Therefore, the findings from these materials are somewhat limited in terms of applicability to the current Sn-Ag-Bi system.

The homologous temperatures, which represent the test (and use) temperatures of the Sn-Ag-Bi are also higher than those experienced by superalloys in an operating jet engine, typically 0.46–0.62.[39] The latter materials rely upon precipitation hardening to maintain their high-temperature strength. Interestingly, the yield stress dependencies on temperature by the superalloys show a trend that is similar to that shown by the Sn-Ag-Cu solder in Fig. 5. Recall that the Sn-Ag-Cu alloy is primarily strengthened by precipitation hardening (Ag_3Sn particles). Again, the behaviors observed in traditional precipitation hardened alloys can have some applicability to the Sn-Ag-Bi solder, but with due regards to (a) different homologous temperature ranges and (b) the presence of the solution-strengthening mechanism.

In summary, although the Ag_3Sn and large Bi particles affect the yield stress behavior of the as-fabricated, Sn-Ag-Bi alloy, the controlling microstructure is the solid-solution Sn(Bi) phase. Solid-solution strengthening remained effective in the Sn-Ag-Bi solder at higher homologous temperatures than would be expected, based on traditional light metal and Ni-based alloys. However, thermal activation quickly allowed dislocation motion to circumvent the solid-solution obstacles with increased temperature. At the upper temperature limit of 160°C, the Sn-Ag-Bi solder yield stress was

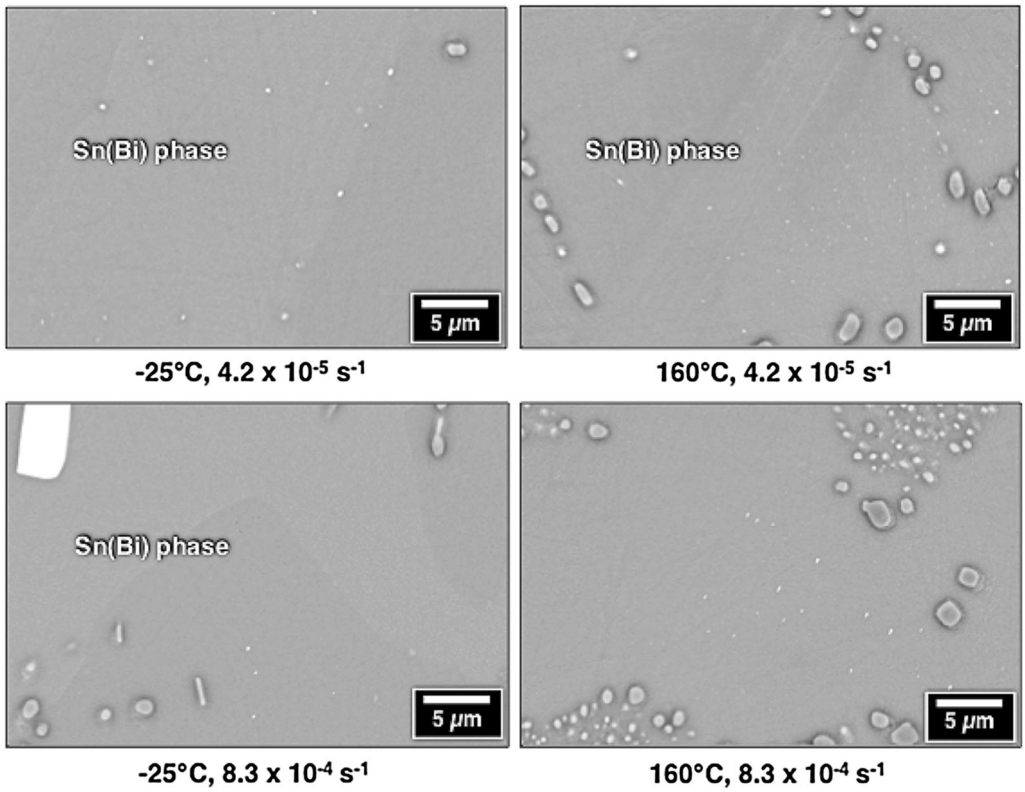

Fig. 20. SEM images show the Sn(Bi) matrix of the Sn-Ag-Bi solder after testing at − 25°C and 160°C and both strain rates. The samples were aged at 150°C for 24 h prior to testing. The BSE image mode and high magnification accentuated the distribution of smaller Bi particles.

similar to that of the Sn-Ag-Cu solder, which relies solely on precipitation hardening.

Post-aged Condition

The yield stress behaviors correlate with the representative starting microstructures: Fig. 1, as-fabricated condition; Fig. 2, aged at 125°C (24 h); and Fig. 3, aged at 150°C (24 h). The microstructure observed in Fig. 2 (125°C aging treatment) predicts that the yield stress remains largely unchanged, not only because the partial resolutionizing of the larger Bi precipitate particles and Bi precipitation in the Sn(Bi) phase were relatively minor, but also because they generate opposite effects—yield stress increase and decrease, respectively. On the other hand, the microstructure observed in Fig. 3, which resulted from the 150°C aging treatment (Fig. 3), causes a decrease in the yield stress due to the partial losses of both precipitation hardening and solution strengthen mechanisms.

Figure 6 compares the yield stress values as a function of test temperature between samples tested in the as-fabricated condition and those post-aged at 125°C. The above prediction was not observed, whereby the 125°C aging treatment leaves the yield stress unchanged. The yield stress was slightly higher at 25°C, 75°C, and 125°C. This trend, which was observed for both strain rates, suggests that the resolutionization of Bi had the greater effect on yield stress. Also, it is important to consider that the aging treatments also lead to recovery processes, which annihilate point defects (vacancies and interstitials) that support thermally activated dislocation motion. Their absence decreases dislocation mobility, thereby raising the yield stress.

The yield stress remained unchanged by the aging treatment at − 25°C and 160°C (Fig. 6). The lack of an effect at − 25°C arose for the same reason proposed earlier—the reduced mobility of existing dislocation and/or the low concentration of existing mobile dislocations. At 160°C, thermal activation assisted dislocation motion to the extent that it overwhelmed the additional strength provided by the resolutionizing of large Bi particles.

The 150°C (24 h) aging treatment caused the starting microstructure to develop coarsened, large Bi particles and the precipitation of Bi particles in the Sn(Bi) solid-solution phase (Fig. 3). The activity of both phenomena predicts a decrease in the yield stress due to a loss of both precipitation hardening and solution strengthening mechanisms. Figure 7 provides a comparison of yield stresses as a function of test temperature. As observed previously, the yield stresses were similar at − 25°C, which an earlier hypothesis attributed to reduced dislocation mobility that was relatively insensitive to microstructural modifications arising from the aging treatment.

At the test temperatures of 25°C and 75°C, the crossover effect dominated the yield stress behavior of the aged samples at both strain rates. Crossover occurred at approximately 30°C and 70°C for the 4.2×10^{-5} s^{-1} and 8.3×10^{-4} s^{-1} strain rates, respectively. The yield stress was *greater* for the 150°C aged samples at 125°C and 160°C, which is inconsistent with the precipitation of Bi particles in the Sn(Bi) solid-solution phase (Fig. 3c). Consideration was given to the potential effects of recovery and recrystallization. Recovery processes during the aging treatment could cause a yield stress increase, but it is inconsistent with the crossover effect. Recrystallization was not observed in the SEM images, including the use of the electron channeling contrast.

Further analysis turned to the Sn-Ag-Cu solder data. Figures 8 and 9, when considered together, address all of the Sn-Ag-Cu and Sn-Ag-Bi yield stress data for the strain rates of 4.2×10^{-5} s^{-1} and 8.3×10^{-4} s^{-1}, respectively. The Sn-Ag-Bi solder exhibited higher yield stresses than the Sn-Ag-Cu solder at both strain rates and for all sample conditions, despite the Bi coarsening and precipitation processes caused by the aging treatment (Fig. 3). However, that yield stress advantage diminished with increasing test temperature, particularly so at the slower strain rate where both alloys eventually exhibited equivalent values at 160°C and the of 4.2×10^{-5} s^{-1} strain rate. An important factor was the *rate* of yield stress loss with temperature. The rate of yield strength loss decreased with increasing test temperature for the Sn-Ag-Cu alloy, regardless of sample condition (and strain rate). The effect was accentuated by the slower strain rate. The Sn-Ag-Cu alloy has only the precipitation hardening mechanism that is attributed to the Ag_3Sn particles. On the other hand, the rate of yield strength loss increased with increasing test temperature for the Sn-Ag-Bi solder, which reflects the loss of the solution strengthening mechanism. Thus, the precipitation hardening mechanism became more important to the Sn-Ag-Bi at the higher temperatures (like the traditional high-temperature superalloys). The crossover effect represents a slowing to the rapid yield stress decline caused by a loss of the solution strengthening mechanism. The added precipitation hardening effect at high temperatures must have originated from coarsening of the large Bi particles and Bi precipitation in the Sn(Bi) phase.

Lastly, the test temperatures represented high homologous temperatures for the Sn-Ag-Bi solder. Therefore, consideration was given to the possible effects of creep deformation, including comparisons to traditional solid-solution alloys.[40–43] The Sn-Ag-Bi solder had its steady-state creep performance described by the sinh law in reference 26. The sinh law exponent, n, was 3.1 ± 0.4 for the as-fabricated condition. This value of n, which does not differ significantly from the power law exponent, indicated Class I "alloy-type" behavior. Class 1 creep deformation is based upon dislocations moving in a sequence of glide and climb steps. In the case of solid-solution alloys, the dislocations are accompanied by the solute atmosphere that must diffuse along with them. The relatively low apparent activation energy (ΔH) of 66 ± 7 kJ/mol, which was calculated in reference 26, implies that the Bi atmosphere has a high mobility, which was also confirmed by the absence of a sigmoidal shape to the strain–time plots in reference 26. That prior creep study included samples exposed to the same aging treatments prior to testing. The aging treatments had only a small effect on values of n and ΔH, which indicates that they caused very little change to the overall deformation process. Therefore, the conclusion was made that any creep deformation, which may have been taking place during the stress–strain tests, had a negligible effect on the yield stress trends observed in Figs. 6 and 7.

Plastic Deformation: Stress–Strain Curves and Microstructures

As-Fabricated Condition

The stress–strain curves were shown in Figs. 10a and 11a that represent tests performed on the as-fabricated Sn-Ag-Bi solder at the two strain rates, 4.2×10^{-5} s^{-1} and 8.3×10^{-4} s^{-1}, respectively. In general, the work hardening rate increased with decreasing temperature. Figures 10b and 11b show that the stress–strain curves obtained at 125°C and 160°C initially experienced work softening, albeit with some variability for the conditions of 125°C and 8.3×10^{-4} s^{-1}. Subsequent work hardening was accompanied by fluctuations. The work softening was generally consistent under all conditions while fluctuations were most prominent at the faster strain rate.

The work softening and fluctuations were attributed to two likely mechanisms. The first mechanism is dynamic recrystallization (DRX).[44,45] The temperatures, 125°C and 160°C, correspond to homologous temperatures of 0.82 and 0.89, respectively, which are well within the recrystallization regime. Figure 10b, which represents the slower strain rate data, showed a softening behavior followed by work hardening—this single cycle variant of DRX is referred to as *continuous* DRX. When fluctuations take place (e.g., Fig. 11b), they suggest multiple cycles of DRX; this behavior is referred to as *cyclic or discontinuous DRX*. A work softening behavior, which was attributed to continuous DRX, was observed during the time-independent deformation of the Sn-Ag-Cu alloy at 125°C and 160°C, but only at the slower strain rate.[22] However, fluctuations were not observed in this alloy. Lastly, both variants of DRX phenomenon have been observed in pure Sn by Thijssen when tested under similar conditions.[46] Therefore, there is strong evidence that DRX can take place in the Sn-Ag-Bi solder.

The work softening can also be interpreted as a second yield point, which together with the subsequent fluctuations, is described by the Portevin–Le Chatelier effect.[47,48] This phenomenon is caused by the atmosphere of solute atoms (Bi) interrupting the movement of dislocations. The drop in stress after the yield point occurs when dislocations break free of the Bi atmosphere. The fluctuations originate from a repetition of the following steps: (a) Bi atmosphere impedes dislocation mobility; (b) there is a build-up of stress on the dislocations from the applied load; and (c) the dislocations break-away from the Bi atmosphere. The fluctuations were relatively weak in Figs. 4b and 5b when compared to the highly serrated, stress–strain curves observed in traditional solution-strengthened alloys because the high homologous temperatures allow thermal activation to contribute to the mobility of the dislocations.

The source of the work softening observed in Figs. 10b and 11b cannot be attributed, conclusively, to either DRX or the Portevin–Le Chatelier effect since it was observed in the Sn-Ag-Cu alloy. Certainly, the behavior could result from a combination of both mechanisms in Sn-Ag-Bi, albeit, microstructural evidence was not documented in the SEM images to support recrystallization. The fluctuations occurred exclusively in the Sn-Ag-Bi alloy, which has the Sn(Bi) solid-solution phase, which supports the Portevin–Le Chatelier effect.

The microstructures were analyzed, which followed the stress–strain tests of the as-fabricated samples. Figures 15, 16 and 17 provide SEM photographs that illustrate microstructural features following plastic deformation at the limiting experimental conditions defined by the two strain rates, 4.2×10^{-5} s^{-1} and 8.3×10^{-4} s^{-1}, as well as the minimum and maximum temperatures, − 25°C and 160°C, respectively. The samples tested at − 25°C and either strain rate did not show significant changes to the microstructure. The absence of shear bands or grain boundary sliding reflected a homogeneity by the deformation, which was anticipated at this relatively high homologous temperature (0.51). Also, primary microstructural features: Ag_3Sn particles, large Bi particles, or the solid-solution Sn(Bi) phase remained unchanged after the nearly 10% strain in the samples.

Microstructural changes were observed after deformation at 160°C and the 4.2×10^{-5} s^{-1} strain rate, which included coarsening of the large Bi particles (upper right-hand image in Fig. 16) and the formation of Bi precipitates in the Sn(Bi) matrix phase (upper right-hand image in Fig. 17). Two scenarios were considered to explain Bi coarsening and precipitation phenomena in Figs. 16 and 17, respectively. The first scenario was that Bi particle coarsening and precipitation resulted simply from an in situ aging of the test specimen caused by the 40-min exposure to 160°C. The second scenario would be deformation-enhanced coarsening and precipitation mechanisms. The latter mechanism proposes that Bi atoms accumulate around dislocations due to the latter's stress field. The local Bi concentration exceeds the solubility limit, giving rise to either the coarsening of the existing large Bi particles or the precipitation of new Bi particles in the Sn(Bi) matrix.

Unfortunately, very little research has been performed on such a phenomenon in low-melting temperature alloys. Strain-assisted coarsening or precipitation has been observed in the deformation of Al-based alloys at similar homologous temperatures.[49,50] However, considerably higher total plastic strains (> 0.3) were executed to observe it. Moreover, Bhat and Laird noted that plastic strain had a limited effect on the further coarsening of pre-existing particles; however, it could *potentially* enhance precipitation. Strain enhanced coarsening has been recorded during the creep deformation of chrome-moly (Cr-Mo) steels and Al alloys.[51–53] Those studies confirmed that the creep strain, not in situ thermal aging, accelerated the coarsening of precipitates. Creep deformation can certainly take place in the Sn-Ag-Bi at − 25°C and 160°C because they represent high homologous temperatures (0.51 and 0.89, respectively).

Strain enhanced coarsening was unlikely in the Sn-Ag-Bi solder. The microstructure was largely unchanged after testing at − 25°C and either strain rate, despite the high homologous temperature and same total strain experienced at 160°C. In a similar regard, strain-assisted coarsening was not observed after testing at 160°C and the faster strain rate (lower right-hand image in Fig. 16) and only a small degree of Bi precipitation was observed in the Sn(Bi) phase (white arrows, lower right-hand image in Fig. 17). Therefore, the large Bi particle coarsening and Bi precipitation observed at 160°C and 4.2×10^{-5} s^{-1} strain rate were more likely caused by in situ aging due to the sample's exposure to 160°C for approximately 40-min.

The large Bi particle coarsening and Bi precipitation in the Sn(Bi) phase potentially affected the stress–strain curves. Negligible fluctuations were observed at the slow strain rate (Fig. 10b, 160°C) in which in situ aging was more likely to cause Bi precipitation in the Sn(Bi) phase. The competing explanation was that thermal activation provided additional support to dislocation mobility at a slower strain rate.

Post-aged Condition

The effect was investigated that the aging treatments had on the post-yield, deformation behavior of the Sn-Ag-Bi solder. Referring to Figs. 12, 13 and 14, both aging treatments caused the work hardening rate to increase versus the as-fabricated condition for tests performed at − 25°C, 25°C, and 75°C. This trend was observed at both strain rates. The stress–strain curves, which were obtained at 125°C

and 160°C, were not altered by either aging treatment versus the as-fabricated condition at the slow strain rate of 4.2×10^{-5} s^{-1}. Under the faster strain rate of 8.3×10^{-4} s^{-1}, similar stress–strain curves were observed between the as-fabricated and post-125°C aging conditions. However, when the aging temperature was raised to 150°C, the work softening phenomenon and fluctuations, which were observed in those prior two sample conditions, were replaced with only work hardening at 125°C and 160°C.

The post-yield point, stress–strain behaviors in Figs. 12, 13 and 14 correlated with the starting (post-aged) microstructures shown in Figs. 2 and 3 for the (24 h) aging treatments at 125°C and 150°C, respectively. Figure 2b and c show that the 125°C aging treatment caused modest resolutionization of large Bi particles and slight Bi precipitation in the Sn(Bi) solid-solution phase. This aging treatment caused an increased work hardening rate at − 25°C, 25°C, and 75°C in both Figs. 12 (4.2×10^{-5} s^{-1}) and 13 (8.3×10^{-4} s^{-1}). Although relatively modest, both phenomena could potentially reduce dislocation mobility, which would increase the work hardening rate. Although not visible in the SEM images, the aging treatment could have been responsible for recovery processes that eliminated point defects (vacancies and interstitials) from the microstructure.[54] These defects assist with thermally activated dislocation motion, which is relevant even for these "lower" test temperatures, given their relatively high, corresponding homologous temperatures. The consequence would also constitute an impediment to dislocation motion, which would increase the work hardening rate.

The analysis examined the stress–strain data obtained at 125°C and 160°C. The 125°C aging treatment had a negligible effect on Sn-Ag-Bi deformation when compared to that observed of samples in the as-fabricated condition and tested at the same two temperatures. Given the trend whereby the aging treatment had a decreasing effect on work hardening with the increasing test temperature (− 25°C to 75°C), it was surmised that thermal activation overwhelmed the aging treatment effects of both Bi solutionization and/or precipitation in the Sn(Bi) phase on dislocation mobility at these very high homologous temperatures.

The effects are considered for 150°C aging treatment. The starting microstructures were characterized by coarsening of the large Bi particles (Fig. 3b) and significant precipitation of Bi particles in the Sn(Bi) solid-solution phase (Fig. 3c). Generally, precipitation events indicate an "overaged" condition in solid-solution alloys. The loss of solute particle coherency increases dislocation mobility and thus, would be predicted to cause a loss of work hardening by a solution strengthening mechanism. The − 25°C, 25°C, and 75°C test temperature data in Figs. 12 and 13 indicate that this scenario was not applicable to the Sn-Ag-Bi alloy. Rather, these data imply that the Bi precipitates in the Sn(Bi) phase were more effective than the solid-solution microstructures towards hindering the thermally activated dislocation motion under these relatively high, homologous temperatures. Recall that this premise underscores the working theory of many precipitation-hardened superalloys.

The analysis considered the stress–strain data obtained at the 125°C and 160°C test temperatures after the 150°C aging treatment. The post-yield point stress–strain curves obtained at 125°C and 160°C were similar to those observed with samples in as-fabricated and post-125°C aged conditions, but only for the slow strain rate. At the fast strain rate, work softening and fluctuations disappeared from the stress–strain curves (Fig. 14). The 150°C aging treatment caused the precipitation of Bi particles from the Sn(Bi) solid-solution phase, which reduced the Bi atoms available to form an atmosphere around dislocations and thus affect their motion per the Portevin–Le Chatelier effect. At the slower strain rate, the Bi atoms, albeit fewer, still affected dislocation mobility, resulting in the retention of work softening and fluctuations. However, at the faster strain rate, dislocations could effectively "outrun" the reduced Bi atmosphere, resulting in an absence of work softening and fluctuations.

The Sn-Ag-Bi microstructures were documented *after* the stress–strain tests. Deformation artifacts—cracks, shear bands, grain boundary movement, etc.—were not observed on any of the post-aged, post-stress–strain tested samples.

The post-deformation microstructures were evaluated belonging to Sn-Ag-Bi samples that were aged at 125°C (24 h) prior to testing. The large Bi particles reappeared to the same extent as in Fig. 16 (as-fabricated condition). A representative microstructure is shown in Fig. 18a that was taken of the sample tested at − 25°C and 4.2×10^{-5} s^{-1}. The precipitate particles were still absent from the Sn(Bi) phase; the same observation was made at the faster strain rate. Figure 18b shows an SEM/BSE image taken of the Sn(Bi) solid-solution phase from the sample tested at 160°C (4.2×10^{-5} s^{-1}). The Bi precipitation was only slightly greater than that observed Fig. 17 (as-fabricated condition) and only a few more particles were observed for the 8.3×10^{-4} s^{-1} strain rate. In situ aging remained as the likely source of Bi precipitation in the Sn(Bi) observed in Fig. 18b. Therefore, the 125°C, 24 h aging treatment did not allow the plastic deformation to significantly alter the Sn-Ag-Bi microstructure more so than was recorded of similarly-tested samples that started in the as-fabricated condition. This point was valid for both strain rates.

The post-deformation microstructure was evaluated from those samples aged at 150°C and 24 h prior to the stress–strain test. Figure 19 highlighted the large Bi particles, which can be compared to the starting microstructure in Fig. 3b. The − 25°C test

(both strain rates) caused an increase in the concentration of large Bi particles. The concentration of large Bi particles slightly exceeded that observed in similarly tested samples that started in the as-fabricated condition (Fig. 16). In situ aging effects were not observed at − 25°C. Therefore, the 150°C aging treatment caused the microstructure to become susceptible to the strain-enhanced coarsening behavior.

Figure 19 also shows the large Bi particle morphologies of samples tested at 160°C. A significant degree of coarsening occurred at both strain rates versus the starting microstructure (Fig. 3b). Recall that in situ aging (≈ 40 min at 160°C) was deemed as the cause of this coarsening in the prior case of as-fabricated samples when tested at the *slow* strain rate (Fig. 16). However, this explanation seems unlike in the aged samples because they were exposed to 150°C for 24 h (1440 min). Given the proximity of 150°C to 160°C, it is unlikely that the additional 40-min exposure to 160°C would have led to further coarsening of the large Bi particles. Moreover, the same degree of coarsening was observed at the faster rate, 8.3×10^{-4} s^{-1}. Therefore, strain-enhanced coarsening took place during deformation at 160°C for both strain rates that followed the 150°C aging treatment.

The SEM images in Fig. 20 show the post-test, Sn(Bi) solid-solution phase as a function of temperature and strain rate for samples aged at 150°C (24 h). An increased variability in Bi precipitation was observed between different Sn(Bi) regions of the same test sample; therefore, the following observations describe only the high-level trends. The specimens, which were tested at − 25°C and either strain rate, exhibited a *reduction* of Bi particles when compared to the as-aged condition (Fig. 3c). The same trend was documented for samples tested at 160°C. These observations imply that the Sn(Bi) phase experienced a strain-enhanced *dissolution* of its Bi component during the deformation. The greatest variability of Bi dissolution between Sn(Bi) regions occurred at 160°C and the fast strain rate, 8.3×10^{-4} s^{-1}. A possible source of this variation was a difference in the degree of deformation between Sn(Bi) regions.

Strain-enhanced dissolution would have its origins in strain (deformation)-enhanced *diffusion*, which has a long history of study in the literature. Ruof and Balluffi examined the role of point, line, and area defects—that is, vacancies, dislocations and grain boundaries, respectively—on dissolution behavior.[55–57] The authors concluded that point vacancies were not produced at a sufficient rate to accelerate diffusion processes and thus, enhance of solute dissolution. Rather, short-circuit diffusion mechanisms supported strain-enhanced diffusion, which included pipe diffusion in dislocations and grain-boundary diffusion.

Ruoff also discussed *mechanical diffusion* in materials.[58] This mechanism is less likely to have taken in the present Sn-Ag-Bi study. First, it typically occurs at strain rates exceeding 10^{-4} s^{-1} and at temperatures equal to, or below, one-half the homologous temperature. Both parameters are outside the current test space. Secondly, mechanical diffusion is based upon atomic transport along inhomogeneous deformation pathways—e.g., shear bands, cell structures, etc. These features were not observed in the Sn-Ag-Bi microstructure.

Numerous authors have considered *heat of mixing* as a mechanism to accelerate the dissolution of second-phase materials.[59,60] Although certainly plausible, direct evidence was not obtained that would confirm this mechanism in the Sn-Ag-Bi alloy.

The stress–strain curves were compared to the post-test microstructures to determine if a correlation existed between the two metrics as a function of aging treatment. Because the Ag_3Sn particle morphology did not change significantly during deformation, regardless of strain rate, the discussion focused on the large Bi particles and Sn(Bi) solid-solution phase features.

The first group of tests results were those obtained at − 25°C, which also represented 25°C and 75°C. The large Bi particles experienced coarsening during the tests at either strain rate, whether aged at 125°C or 150°C. The Sn(Bi) phase microstructure was largely unchanged for the sample aged at 125°C, but underwent stain-enhanced dissolution of the Bi particles after aging at 150°C. Either of these two phenomena would have contributed in situ to the increased work hardening rates observed in Figs. 12 and 13.

The analysis examined the performance at the test temperature of 160°C, which is representative of the 125°C test results. The stress–strain curves were largely unchanged by the 125°C, 24 h aging treatment (Figs. 12, 13 and 14) at either strain rate. Large Bi particle coarsening occurred simultaneously with Bi precipitation in the Sn(Bi). Both processes would lead to enhanced precipitation hardening, which is predicted to increase the work hardening rate at high homologous temperatures. However, this trend was not observed in the stress–strain curves. The conclusion was made that the precipitation hardening effect was circumvented by the increased contribution of thermal activation to dislocation motion.

The 125°C and 160°C stress–strain curves exhibited a complex relationship versus the microstructure, which developed during deformation, when the Sn-Ag-Bi alloy was aged at 150°C (24 h). More specifically, the complicating factor was strain rate. At the slow strain rate, large Bi particle coarsening and strain-enhanced dissolution of Bi into the Sn(Bi) phase both did not alter work softening and fluctuations that were observed with similarly tested samples in the as-fabricated condition. However, these same phenomena were lost at the faster strain rate (Fig. 17), having been replaced with

work hardening. Therefore, the Portevin–Le Chatelier effect was lost at the fast strain rate for samples exposed to the 150°C aging treatment (Fig. 3c), despite the stain-enhanced dissolution effect that placed Bi back into Sn(Bi) solid solution phase during the plastic deformation. Therefore, the latter behavior had a lesser effect than did the precipitation of Bi caused by the aging treatment.

The findings are briefly summarized, from the above analysis that sought to correlate the stress–strain curves of the Sn-Ag-Bi solder with the microstructural features documented prior to, and upon completion of, the deformation. At the low test temperatures of − 25°C, 25°C, and 75°C, the aging treatments led to a consistent trend of increasing the work hardening rate, which was unaffected by the microstructural changes that took place during deformation, regardless of strain rate. When the test temperatures were raised to 125°C and 160°C, the stress–strain curves were not significantly altered by the 125°C aging treatment and its changes to the starting microstructure. Microstructural changes were relatively minor during deformation and strain rate was not a factor. The 150°C aging treatment established a starting microstructure that resulted from the coarsening of the large Bi particles and significant Bi precipitation in the Sn(Bi) phase. This aged microstructure allowed strain-enhanced coarsening of the large Bi particles and the dissolution of Bi phase back into the Sn(Bi) solid-solution phase during deformation. The latter mechanism could not fully compensate for the extent of Bi precipitation in Sn(Bi) caused by the aging treatment. The deformation retained the Portevin–Le Chatelier effect, but only at the slower strain rate due to the reduced concentration of Bi in solid-solution.

SUMMARY

1. This study documented the yield stress and plastic deformation behavior of the 91.84Sn-3.33Ag-4.83Bi (wt.%, abbreviated Sn-Ag-Bi) solder. These properties correlated with the microstructures using the scanning electron microscope (SEM).
2. The specimens were tested at two strain rates: 4.2×10^{-5} s^{-1} and 8.3×10^{-4} s^{-1}. The test temperatures ranged from − 25°C to 160°C. Samples were tested in the as-fabricated condition as well as following a 24-h aging treatment at either 125°C and 150°C.
3. The Sn-Ag-Bi yield stress decreased monotonically with increased test temperature at both strain rates and all sample conditions. Dislocation activity (mobility and/or the concentration of mobile species) was limited at lower test temperatures, which reduced the strain-rate sensitivity.
4. The 125°C aging treatment caused some resolutionizing of the larger Bi precipitates and a small degree of Bi precipitation in the Sn(Bi) solid-solution phase. The aging treatment caused an increase to the yield stress at 25°C, 75°C, and 125°C, but left it unchanged at − 25°C and 160°C for both strain rates.
5. The 150°C aging treatment caused coarsening of both Ag_3Sn the large Bi particles as well as the precipitation of Bi particles in the Sn(Bi) solid-solution phase. At both strain rates, the yield stress showed a crossover effect at approximately 30°C and 70°C for the 4.2×10^{-5} s^{-1} and 8.3×10^{-4} s^{-1} strain rates, respectively. Yield stress values were reduced below the crossover point and increased above it, relative to the as-fabricated condition.
6. The post-yield point, stress–strain curves of the *as-fabricated* samples showed work hardening at − 25°C, 25°C, and 75°C. A work softening behavior was observed at 125°C and 160°C and both strain rates; the likely mechanisms were continuous DRX, the Portevin–Le Chatelier effect, or a combination of the two behaviors. Fluctuations, which were superimposed on the work hardening, were attributed to the Portevin–Le Chatelier effect.
7. The post-yield point, stress–strain curves of *aged* samples exhibited an increase to the work hardening rate at − 25°C, 25°C, and 75°C, the magnitude of which, generally diminished with increasing test temperature. This trend was insensitive to the aging temperature and displayed only minor difference between strain rates.
8. When tested at 125°C and 160°C, the as-fabricated and 125°C (24 h) aged samples exhibited similar post-yield point, stress–strain curves that did not differ between strain rates. Increasing the aging temperature to 150°C did not affect the stress–strain curves at the slow strain rate. However, the stress–strain curves lost the Portevin–Le Chatelier effect—work softening and fluctuations—at the fast strain rate despite the strain-enhanced Bi dissolution in the Sn(Bi) phase during deformation.
9. The microstructures, which followed the plastic deformation did not exhibit deformation features such as shear bands, voids, or cracks *across all test conditions*.
10. Accelerated aging tests and service conditions require the Sn-Ag-Bi alloy to perform at very high homologous temperatures. Therefore, precipitation hardened and solution-strengthening principles obtained from traditional alloys cannot be easily mapped to Sn-Ag-Bi stress–strain behavior. Nevertheless, the present study confirmed that very limited degradation can be expected from the

yield stress and plastic deformation properties of the Sn-Ag-Bi alloy when exposed to high homologous temperatures prior to, or during, time-independent deformation.

ACKNOWLEDGMENTS

The authors wish to thank Brian Wroblewski for a thorough review of the manuscript. Sandia National Laboratories is a multi-mission laboratory managed and operated by National Technology and Engineering Solutions of Sandia LLC, a wholly owned subsidiary of Honeywell International Inc. for the U.S. Department of Energy's National Nuclear Security Administration under contract DE-NA0003525. This paper describes objective technical results and analysis. Any subjective views or opinions that might be expressed in the paper do not necessarily represent the views of the U.S. Department of Energy or the United States Government.

REFERENCES

1. P. Snugovsky, S. Bagheri, M. Romansky, D. Perovic, L. Snugovsky, and J. Rutter, *J. Surf. Mount Technol.* 25, 42 (2012).
2. P. Vianco and J. Rejent, US Patent 5,439,639 (1995).
3. P. Vianco and J. Rejent, *J. Electron. Mater.* 28, 1131 (1999).
4. P. Vianco and J. Rejent, *J. Electron. Mater.* 28, 1139 (1999).
5. P. Vianco, I. Artaki, and A. Jackson, in *Proceedings of Surface Mount International Conference* (1994), pp. 437–448.
6. I. Artaki, D. Finley, A. Jackson, U. Ray, and P. Vianco, in *Proceedings of Surface Mount International Conference* (1995), pp. 495–500.
7. P. Vianco and P. Mizik, in *Proceedings of 7th International Sample Materials Processes Electronics Conference* (1994), pp. 366–380.
8. P. Vianco, J. Rejent, I. Artaki, U. Ray, D. Finley, and A. Jackson, in *Proceedings of 46th Electronic Components and Technology Conference* (1996), pp. 1172–1183.
9. P. Snugovsky, S. Bagheri, M. Romansky, D. Perovic, L. Snugovsky, and J. Rutter, *J. SMTA* 25, 32 (2012).
10. M. Sampathkumar, S. Rajesnayagham, S. Ramkumar and S. Anson, in *Proceedings of Surface Mount Technology Association International Conference* (2005), pp. 568–575.
11. P. Vianco, J. Rejent, I. Artaki, and U. Ray, in *Proceedings of IPCWorks'99* (1999), pp. S-03-3–S-03-19.
12. A. Delhaise, P. Snugovsky, I. Matijevic, J. Kennedy, M. Romansky, D. Hillman, D. Adams, S. Meschter, J. Juarez, M. Kammer, I. Straznicky, L. Snugovsky, and D. Perovic, in *Proceedings of the International Conference on Soldering and Reliability* (2017), pp. 576–585.
13. I. Matijevic, Masters of Sci. thesis, University of Toronto, Toronto, Ontario, Canada, 2016.
14. Z. Hai, J. Zhang, C. Shen, E.K. Snipes, J.C. Suhling, M.J. Bozack, and J.L. Evans, *J. Surf. Mount Technol.* 27, 11 (2014).
15. P. Vianco and C. May, in *Proceedings of Surface Mount International Conference* (1995), pp. 481–496.
16. P. Vianco, A. Kilgo, and R. Grant, *J. Electron. Mater.* 24, 1493 (1995).
17. M. McCormack, H. Chen, G. Kammlott, and S. Jin, *J. Electron. Mater.* 26, 954 (1997).
18. M. Ribas, A. Kummar, D. Kosuri, R. Raghu, R. Rangaraju, P. Choudhury, S. Telu, and S. Sarkar, in *Proceedings of SMTA International Conference* (2017), pp. 201–205.
19. H. Hata, Y. Maruya, and I. Shohji, *Mater. Trans. Jpn. Inst. Met.* 57, 887 (2016).
20. D. Pierce, S. Sheppard, A. Fossum, P. Vianco, and M. Neilsen, *J. Electron. Packag.* (2008). https://doi.org/10.1115/1.2837513.
21. M. Neilsen and P. Vianco, *J. Electron. Packag.* (2014). https://doi.org/10.1115/1.4026851.
22. P. Vianco, J. Rejent, and A. Kilgo, *J. Electron. Mater.* 32, 142 (2003).
23. P. Vianco, J. Rejent, and A. Kilgo, *J. Electron. Mater.* 33, 1389 (2004).
24. P. Vianco, J. Rejent, and A. Kilgo, *J. Electron. Mater.* 33, 1473 (2004).
25. P. Vianco, J. Rejent, A. Fossum, and M. Neilsen, *Lead-Free Electronic Solders*, ed. K. Subramanian (New York: Springer, 2006), p. 93.
26. P. Vianco, J. Rejent, M. Grazier, and A. Kilgo, *Materials* 5, 2151 (2012).
27. D. Witkin, *J. Electron. Mater.* 41, 190 (2012).
28. D. Witkin, in *Proceedings of IPC APEX EXPO Conference and Exhibition* (2013), pp. 540–560.
29. Standard Test Methods for Compression Testing of Metallic Materials at Room Temperature: ASTM E9-89A (ASTM, West Conshohocken, 1995), pp. 101–103.
30. Standard Test Methods for Young's Modulus, Tangent Modulus, and Chord Modulus: ASTM E111-82 (ASTM, West Conshohocken, 1995) pp. 1–7.
31. A. de Silva Scari, B. Pockszevnicki, J. Junior, and P. Junior, *J. Struct.* (2014). https://doi.org/10.1155/2014/387680.
32. J. Embury, D. Lloyd, and T. Ramachandran, *Aluminum Alloys: Contemporary Research and Applications*, ed. A. Vasudevan and R. Doherty (Cambridge: Academic Press, 1989), pp. 579–601.
33. O. Ryen, O. Nijs, E. Sjolander, B. Holmedel, H.-E. Ekstrom, and E. Nes, *Metal. Mater. Trans. A* 37A, 1999 (2006).
34. C. Caceres and D. Rovera, *J. Light Met.* 1, 151 (2001).
35. T. Tanaka and S. Watanabe, *Acta Metall. Mater.* 19, 991 (1971).
36. H. Suga, Y. Sueki, M. Higuchi, and T. Imura, *Jpn. J. Appl. Phys.* 15, 379 (1976).
37. L. Gao, R. Chen, and E. Han, *J. Alloy Compd.* 472, 234 (2009).
38. H. Roth, C. Davis, and R. Thomson, *Metall. Mater. Trans. A* 28A, 1329 (1997).
39. M. Donachie and S. Donachie, *Superalloys, a technical guide*, 2nd ed. (West Conshohocken: ASM, International, Materials Park, 2002), pp. 1–9.
40. F. Mohamed, *Mater. Sci. Eng.* 38, 73 (1979).
41. F. Mohamed, K. Murty, and J. Morris, *Metall. Trans. A* 4, 935 (1973).
42. S.-W. Chung, H. Watanabe, W.-J. Ki, and K. Higashi, *Mater. Trans. Jpn. Inst. Met.* 45, 1266 (2004).
43. P. Chaudhury and F. Mohamed, *Metall. Trans. A* 18A, 2105 (1987).
44. T. Sakai and J. Jones, *Acta Metall. Mater.* 32, 189 (1984).
45. H. McQueen, *Mater. Sci. Eng. A* 387–389, 203 (2004).
46. F. Thijssen, Ph.D. thesis, Utrecht University, 2004.
47. A. Yilmaz, *Sci. Technol. Adv. Mat.* (2011). https://doi.org/10.1088/1468-6996/12/6/063001.
48. W. Ozgowicz and B. Grzegorcyk, *J. Achiev. Mater. Man. Eng.* 31, 281 (2008).
49. M.-S. Tsai, P.-L. Sun, P.-W. Kao, and C.-P. Chang, *Mater. Trans.* 50, 771 (2009).
50. S. Bhat and C. Laird, *Acta Metall. Mater.* 27, 1861 (1979).
51. T. Nakajima, S. Spigarelli, E. Evangelista, and T. Endo, *Mater. Trans. Jpn. Inst. Phys.* 44, 1802 (2003).
52. S. Spigarelli, E. Cerri, P. Bianchi, and E. Evangelista, *Mater. Sci. Technol.* 15, 1433 (1999).
53. T. Nakajima, M. Takeda, and T. Endo, *Mater. Trans. Jpn. Inst. Phys.* 47, 1098 (2006).
54. P. Shewmon, *Transformations in Metals* (New York: McGraw-Hill, 1969), pp. 314–315.
55. R. Balluffi and A. Ruoff, *J. Appl. Phys.* 34, 1634 (1963).
56. A. Ruoff and R. Balluffi, *J. Appl. Phys.* 34, 1848 (1963).
57. A. Ruoff and R. Balluffi, *J. Appl. Phys.* 34, 2862 (1963).
58. A. Ruoff, *J. Appl. Phys.* 38, 3999 (1967).

59. N. Vo, S. Odunuga, P. Bellon, and R. Averback, *Acta Mater.* 57, 3012 (2009).
60. J. Guo, J. Rosalie, R. Pippan, and Z. Zhang, *Scr. Metall. Mater*. 13341 (2017).